



School of Chemistry

Optimisation of a Pulsed Direct Current Plasma Enhanced Chemical Vapour Deposition (PDC PE-CVD) Reactor for Growth of Isotopically Pure ^{13}C Diamond Thin Films

Amelia Billings

April 2019

**This thesis is submitted in partial fulfilment of the requirements for the
Honours Degree of MSci (Bsc) at the University of Bristol**

Supervisor: Dr Neil Fox

Second Assessor: Professor Paul May

Physical and Theoretical Group

Contents

Abstract.....	1
Acknowledgements.....	2
Chapter 1: Introduction.....	3
1.1 Diamond: The structure, bonding and effect of carbon-isotope composition on its properties	3
1.2 Technological applications of isotopic diamond.....	5
1.2.1 Beta-voltaic batteries.....	5
1.2.2 Pressure sensors	6
1.3 Plasma enhanced deposition methods for CVD diamond	7
1.3.1 The growth mechanism	7
1.3.2 Microwave Plasma Enhanced CVD (MW PE-CVD).....	9
1.3.3 Pulsed DC Plasma Enhanced CVD (PDC PE-CVD).....	10
1.4 Optimisation: The Taguchi method	11
1.5 Techniques for characterisation of CVD diamond thin films and growth analysis	13
1.5.1 Raman and Infrared (IR) spectroscopy.....	13
1.5.2 Scanning Electron Microscopy (SEM) and Transmission Electron Microscopy (TEM).....	16
1.5.3 Optical Emission Spectroscopy (OES).....	18
1.5.4 Nano-scale Electron Spectroscopy for Chemical Analysis (NanoESCA).....	20
1.6 Project aims	21
Chapter 2: Methodology.....	24
2.1 The PDC PE-CVD reactor set-up.....	24
2.2 Taguchi optimisation.....	25
2.2.1 Design of the orthogonal array	25
2.2.2 Cleaning and growth runs	25
2.3 Characterisation	26
Chapter 3: Results and Discussion	27
3.1 Installation of the ground electrode water-cooling jacket and modifications to the reactor	27
3.2 Optimisation and characterisation of the diamond thin films.....	29
3.2.1 Analysing the Taguchi runs.....	29
3.2.2 Optimisation for Highest Quality Diamond (HQD) growth conditions	35
3.2.3 Optimisation for highest growth rate (HGR) conditions	40
3.2.4 Analysis of the optimised HQD and HGR growth runs by OES	44
Chapter 4: Conclusion and Future Work.....	45
Appendix.....	47
References	51

Abstract

The motivation to grow isotopically pure ^{13}C diamond thin films is in the development of ^{14}C diamond for beta-voltaic batteries, for long-lasting, low power emission. A Pulsed Direct Current Plasma Enhanced Chemical Vapour Deposition (PDC PE-CVD) reactor was optimised by the Taguchi method, for high quality diamond thin films with high growth rate conditions, for the purpose of growing ^{13}C diamond thin films under closed cycle conditions.

The control parameters for the optimisation were power, pressure, pulse frequency, methane concentration and argon concentration, and these were each tested at 4 set-level values. The 16, 1 hour Taguchi growth runs, from an Ar/H₂/CH₄ gas mixture, were conducted post modification of the water-cooling system to the reactor. The substrates were analysed by Raman spectroscopy, Scanning Electron Microscopy (SEM) and Optical Emission Spectroscopy (OES).

The results of the analysis showed that both the quality of diamond growth and the growth rate were improved by the optimisation. The optimised conditions for highest quality diamond growth were as follows: 130 Torr, 4.15 kW, 150 kHz, 3.7% [CH₄], and 3.7% [Ar]. The optimised conditions for highest growth rate were as follows: 130 Torr, 3.85 kW, 125 kHz, 3.7% [CH₄], and 3.7% [Ar]. The highest quality diamond produced, assessed by the Raman spectra, displayed a full line-width at half maximum of 15 cm^{-1} for the peak at 1332 cm^{-1} , characteristic to diamond, and a ratio of the amorphous carbon peak intensity to diamond peak intensity of 0.2. The highest growth rate, determined by the SEM images, was $9.8 \pm 3.7\ \mu\text{m h}^{-1}$.

Acknowledgements

Firstly, I would like to thank Dr Neil Fox for his guidance, expertise and time throughout this project. Thank you for sharing your interesting ideas and thoughts on the diamond growth and reactor modifications, I have enjoyed exploring these throughout the project.

Secondly, I'd like to thank Dominic Palubiski for all his time spent supervising and teaching me the ways of the reactor, organising the parts necessary for the reactor modifications, helping me fix the surprise water leaks and for taking excellent SEM images of the many diamond samples. I greatly appreciate all the help and advice you have given me throughout the project and for making it a fun experience.

Thirdly, I would like to thank James Smith for your supervision in the lab, for your help modifying the reactor, and coming to the rescue resetting the Raman instrument on many occasions.

Finally, I would like to thank Professor Paul May for your interest in the project and advice from start to finish, and the rest of the Bristol University Diamond Group for making me feel so welcome during my brief time spent as a member of the group.

Chapter 1: Introduction

1.1 Diamond: The structure, bonding and effect of carbon-isotope composition on its properties

Diamond is an allotrope of carbon in which the atoms are covalently bonded in a tetrahedral geometry forming a very strong, stable giant covalent lattice structure (see **Figure 1**). The body-centred cubic structure comprises of sp^3 hybridised carbon-carbon bonds. Diamond occurs naturally in an isotopic composition comprising of 98.9% ^{12}C and 1.1% ^{13}C (^{14}C content is negligible),^[1] primarily formed deep in the mantle of the Earth's core in which the temperature and pressure conditions are sufficiently extreme (temperature = 900-1400°C, pressure = 5-6 GPa).^[2]

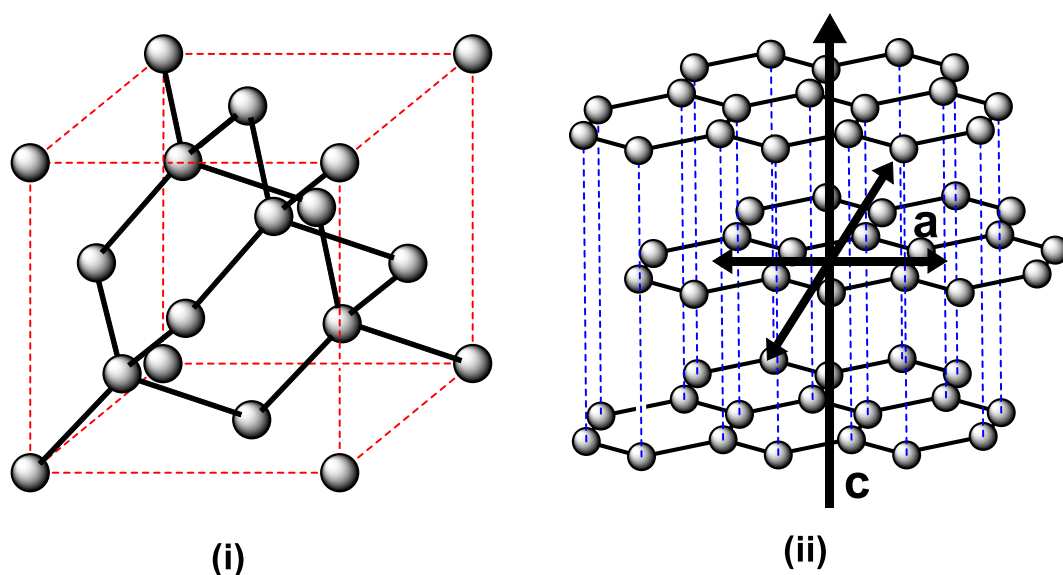


Figure 1. (i) Cubic structure of diamond, (ii) Stacked, layered structure of graphite. Blue dashed lines represent the van der Waals interactions between layers, black arrows indicate the *a*-axis and *c*-axis of the graphite planes.

Synthetic diamond can be grown by Chemical Vapour Deposition (CVD), in which the isotopic composition can be controlled, allowing for isotopically pure¹ ^{12}C or ^{13}C diamond to be grown. The conditions for growth can vary significantly (temperature = 250-1200°C, pressure = 0.01-100 Torr) depending on the type of CVD used.^[3]

Table 1 compares several impressive properties of natural diamond, isotopically pure ^{12}C diamond and isotopically pure ^{13}C diamond, to highlight the effect that varying the isotope composition has on the properties of diamond.

¹ As the ^{13}C and ^{12}C isotope content in the isotopically enriched ^{12}C and ^{13}C diamond is negligible (0.07% and 0.4% respectively), the isotope content can be taken as 'pure'.

Table 1. Properties of carbon allotropes with varying isotopic composition.

Material	Isotopic Content	Properties					
		Atomic Density (10^{-23} Atoms cm^{-3})	Thermal Conductivity ^a ($\text{W cm}^{-1} \text{K}^{-1}$)	Resistivity ($\Omega \text{ m}$)	Indirect Energy Bandgap ^b (eV)	Mohs Hardness ^c	Young's Modulus (GPa)
Natural diamond, Type IIa	98.9% ^{12}C , 1.1% ^{13}C	1.7625 ^[4]	21.9 ^[5]	10^{-12} ^[6]	5.47 ± 0.005 ^[7]	10 ^[6]	1050 ^[8]
Synthetic ^{12}C diamond	99.93% ^{12}C , 0.07% ^{13}C	-	33.2 ^[5]	-	-	-	-
Synthetic ^{13}C diamond	0.4% ^{12}C , 99.6% ^{13}C	1.7632 ^[4]	-	-	5.484 ± 0.005 ^[9]	-	-
Graphite	-	1.136 ^[10]	1.5 ^[6]	3×10^{-3} ^d 4×10^{-6} ^{e[6]}	-	1 ^[6]	25.5 ^[11]

(^a) at $T = 298 \text{ K}$, (^b) at $T = 295 \text{ K}$, (^c) Scale 1-10 (10 is the hardest), (^d) c -axis, (^e) a -axis.

Isotopically pure ^{12}C diamond has been reported to have the highest thermal conductivity (K) of any known material.^[5] This can be explained in terms of phonons, which conduct heat in semi-conducting materials such as diamond. K can be described by the relationship between specific heat capacity (C), the phonon velocity (V), and the phonon mean-free path (λ), shown by **Equation (1)**.^[12]

$$K = \frac{1}{3} \lambda CV \quad (1)$$

The significant increase in the value of K for ^{12}C diamond compared to natural diamond is dominated by the λ term, as C and V are only slightly affected by a change in isotope composition. The effect of λ on K is not well understood, but it was suggested by J.W. Bray and T.R. Anthony^[13] that a decrease in phonon-isotope scattering lead to the significant increase in K , as the isotopic purity increased and lattice defects decreased. Despite there being no reported work on the thermal conductivity of ^{13}C diamond, it can be assumed that the same principles for ^{12}C diamond can be applied to ^{13}C diamond, and that the value for K would be significantly higher than that of natural diamond. Due to the impressive thermal conductivity of the material, diamond composites have been used as superior heat sinks for the electronic industry.^[14,15]

As natural diamond and isotopically pure ^{13}C diamond have large electronic bandgap energies, this presents the material as a good alternative to silicon as a semiconductor.^[16,17] The slight increase in the indirect bandgap energy as the isotope purity increases from natural composition to $\geq 99\%$ ^{13}C content is due to the increase in the lattice volume with increasing isotopic mass, and a change in electron-phonon coupling.^[9,18]

As the isotopic purity increases, there is a decrease in atomic size variation, and less defects occur in

the lattice. It has been reported that isotopically pure ^{13}C diamond has a slightly increased atomic density compared to natural diamond,^[4] as the atomic lattice becomes more regular and atoms are more closely packed. On this basis, it can be expected that the atomic density of isotopically pure ^{12}C diamond would also be slightly larger than that of natural diamond.

It is evident by comparing properties of graphite to diamond (see **Table 1**) that the properties of carbon allotropes can vary significantly depending on the type of bonding between carbon atoms in the structures. Each carbon atom in diamond is covalently bonded to four other carbon atoms, creating the rigid tetrahedral network. Conversely, each carbon atom in graphite is covalently bonded to three other carbon atoms, and the layers bound by weak van der Waals interactions (**Figure 1**). Despite the weaker $\text{sp}^3\text{-sp}^3$ carbon-carbon bonds in diamond (calculated energy = $82.76 \text{ kcal mol}^{-1}$ ^[19]) compared to the intralayer $\text{sp}^2\text{-sp}^2$ carbon-carbon bonds in the graphite layers (calculated bond energy = $91.58 \text{ kcal mol}^{-1}$ ^[19]), it is the weak van der Waals interactions (calculated binding energy = $1.3 \text{ kcal mol}^{-1}$ ^[20]) between layers in graphite which make it easily susceptible to mechanical and thermal deformation, as significantly less energy is required to break the layers apart. This results in a much lower value for the Young's modulus of graphite, and a value of 1 on the Moh's hardness scale, compared to diamond which has the highest known values for both. Furthermore, graphite has a significantly lower resistivity compared to diamond, due to the delocalisation across the layer planes of a non-bonding valence electron for each carbon atom in graphite.

1.2 Technological applications of isotopic diamond

1.2.1 Beta-voltaic batteries

By 2025, the UK is estimated to have $\approx 260,000$ tonnes of radioactive graphite waste from the casing of fuel rods for nuclear reactors.^[21] This poses concerns over the safe-handling, storage and disposal of the waste which contains a high percentage of the radioactive ^{14}C isotope. Research conducted at the Bristol Cabot Institute in 2016^[22] showed that by thermal decomposition of the graphite, the ^{14}C could be removed and stored in gas form, which would considerably reduce the radioactivity of the waste. The ^{14}C could then be used as a carbon feedstock for diamond to create a novel beta-voltaic battery or so-called 'nuclear battery'.^[23,24] Diamond has been used before as a semi-conducting material for components in beta-voltaic batteries,^[25,26] but there has been no published work to date using ^{14}C diamond, as the prototypes by the Bristol Cabot Institute are still in early development.

The process of energy release would occur by beta emission upon ^{14}C decay, which produces a stable isotope of nitrogen and a beta particle with energy of $\approx 50 \text{ keV}$. As the beta particles collide with other carbon atoms in the diamond, electron-hole pairs are created, and an electric current is generated as delocalised electrons flow toward the metal electrode-diamond interface.

The appeal of creating these batteries is not only to remove some of the radioactive waste produced by nuclear reactors, but to create a low power, long-lasting device, in which the energy conversion has a half-life spanning 5700 years. Despite the low energy emission ($\approx 15 \text{ J g}^{-1}$ of ^{14}C per day), the ^{14}C diamond would have high energy density, and the power capacity could be maximised by placing the cells in series. These devices would be useful for application in remote areas such as on spacecraft, underground or mountainous regions, and once encased in standard diamond, the batteries would be safe to be used in the body for pacemakers.

Growth of ^{13}C diamond by CVD with a $^{13}\text{CH}_4$ feedstock, followed by transmutation in a specialised facility, would offer a method of producing ^{14}C diamond for design, development and study of beta-voltaic battery prototypes. This would be more economical and feasible than obtaining radioactive graphite waste from the nuclear industry.

1.2.2 Pressure sensors

Diamond anvil cells (DACs) are used to create well-controlled high-pressures and temperatures as a means of measuring and testing the physical properties of various materials.^[27,28] Temperatures of up to 1200 K and pressures of up to 25 GPa can be achieved, testing both liquid and solid samples. Infrared and Raman spectroscopy can be used to study the radiation emitted from the sample as pressure and temperature is varied, and X-ray diffraction can be used to measure the crystallographic structure. Diamond is used in the cell to compress the sample, as it is chemically inert and has high compressive strength.

Due to the distinct difference in Raman shift between ^{13}C and ^{12}C (refer to section 1.5.1), and the dependence of the ^{13}C Raman shift with respect to temperature and pressure changes, isotopically pure ^{12}C and ^{13}C diamond thin films can be used in combination to act as pressure sensors in DACs.^[29,30] Furthermore, a shear-DAC has been reported to successfully transform ^{13}C graphite into ^{13}C diamond by subjecting the graphite to a pressure of 25 GPa in the cell, which offers an interesting alternative method of creating ^{13}C diamond, as opposed to the more traditional approach by CVD.^[31]

1.3 Plasma enhanced deposition methods for CVD diamond

1.3.1 The growth mechanism

There are two main techniques used for diamond growth: the High Pressure, High Temperature (HPHT) technique for large single crystal growth, and CVD for polycrystalline diamond film growth. Diamond growth by CVD relies upon the activation of carbon-containing gaseous species, and the subsequent deposition onto a substrate surface. The mechanism of growth is well-understood, and has been widely studied.^[3,32-35] Several key points are common amongst the theories: hydrogen must be in abundance to grow diamond successfully, the optimum temperature for diamond growth is $\approx 950^{\circ}\text{C}$, and low carbon concentration ($\approx 2\%$) in a hydrogen atmosphere is necessary.^[33]

Plasma enhanced CVD methods allow growth at lower temperatures than could be achieved by CVD,^[36] and the basic diamond growth mechanism can be explained by considering a typical growth using a gas mixture of hydrogen and a carbon-containing species such as methane. As the gaseous hydrogen and methane diffuse toward the substrate after injection into the reactor chamber, the gases are dissociated by the energy supply (e.g. a hot filament or glow discharge^[37,38]) into reactive fragments and radicals, such as CH_3 , CH_2 , CH and H . The reactive species can adsorb onto the substrate surface, and diamond growth can begin if the adsorbed species remain on the surface long enough for subsequent reactions to occur, with other fragments or radicals in the plasma and on the surface. Alternatively, the reactive species can desorb before further reactions can occur, or not adsorb at all and remain in the plasma.^[32]

The primary roles of hydrogen radicals are as follows: to aid dissociation of long chain hydrocarbon species by high energy collisions in the plasma, to terminate immobilised reactive carbon radicals on the growing diamond surface, known as 'dangling bonds', and to etch graphite from the growing diamond surface.^[32] Kinetically energetic H radicals are produced by electron impact dissociation of hydrogen molecules in the plasma, in which electrons impart an excess of energy required to overcome the bond dissociation energy between hydrogen atoms in a molecule.^[3]

The standard growth model is shown by the schematic diagram in Figure 2. H radicals create dangling bonds by reacting with terminal hydrogen atoms on the surface of the growing diamond. A CH_3 radical, created by dissociation of CH_4 by electron impact or by reaction with H radicals in the plasma, forms a bond with the vacant carbon dangling bond site. Once the same process repeats on a nearby carbon along the growing diamond chain, one dangling methyl radical can attack an adjacent branched methyl group to create a new carbon-carbon bond. The substrate surface and the reactive species in the plasma are part of a dynamic system, in which radicals are continuously being adsorbed and desorbed before reactions are successful.

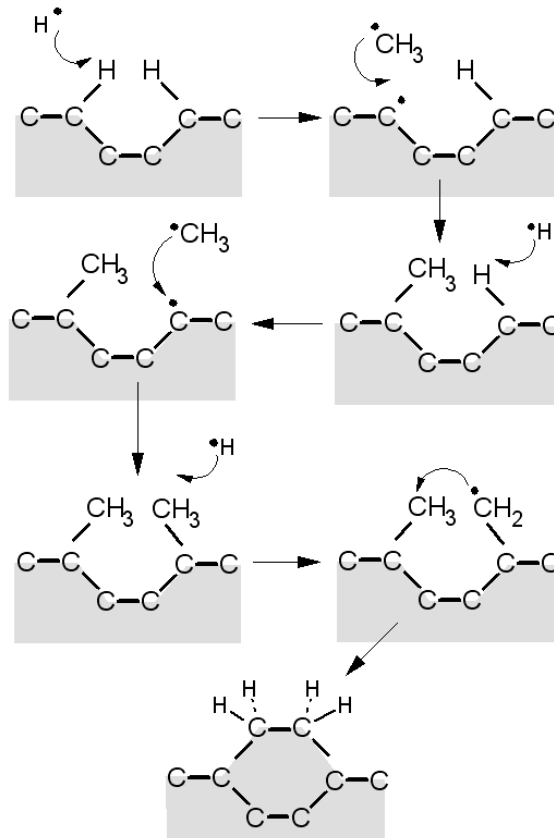


Figure 2. Simple schematic diagram of the standard growth model for CVD diamond.^[32]

Addition of argon into the gas mixture during CVD diamond growth has shown to increase the growth rate of diamond^[39-41] and the substrate temperature uniformity.^[42] As thermal conductivity is inversely proportional to the root of molecular weight,^[43] hydrogen and methane have significantly higher thermal conductivity compared to argon. This means argon molecules are less effective at dissipating the heat away from the plasma, which indirectly increases the gas temperature and encourages dissociation of hydrogen and methane, as observed by Zhu *et al.*^[44] Even a small addition of argon to a hydrogen atmosphere can have a significant effect on the thermal dissipation of the gas.^[45]

Diamond is metastable at the low pressure that is required for growth by CVD: the material is thermodynamically unstable with respect to graphite but kinetically stable due to the high energy barrier to activation, which prevents its spontaneous transformation into graphite.^[46] **Figure 3** shows the phase diagram of carbon, which highlights the unique conditions of CVD diamond growth from those of the HPHT process and naturally occurring diamond.

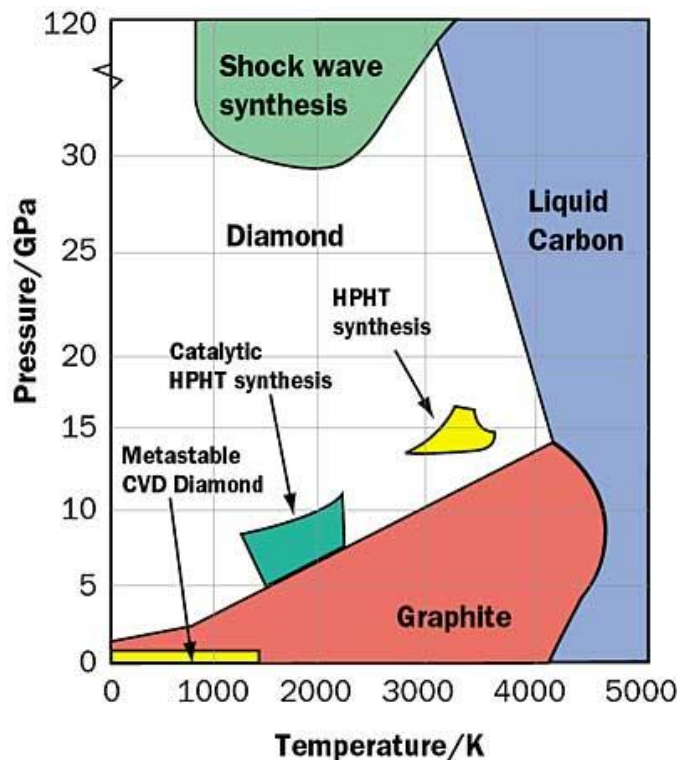


Figure 3. Phase diagram of carbon (from Bundy (1980),^[47] edited by Rantala (2002)^[48]).

1.3.2 Microwave Plasma Enhanced CVD (MW PE-CVD)

MW PE-CVD reactors have been widely used for growth and study of single crystal diamond and polycrystalline diamond thin films from highly stable, dense plasmas.^[49–52]

Figure 4 shows a schematic diagram of a MW PE-CVD reactor set-up which was used to grow nanocrystalline diamond thin film and carbon nanotubes from a H_2/CH_4 gas mixture.^[53] A magnetron generates microwaves with a frequency of 2.45 GHz and power of 1.5 kW, which activate the carbon-containing gas species and dissociate the hydrogen molecules into H radicals, to create a ball-shaped plasma above the substrate.

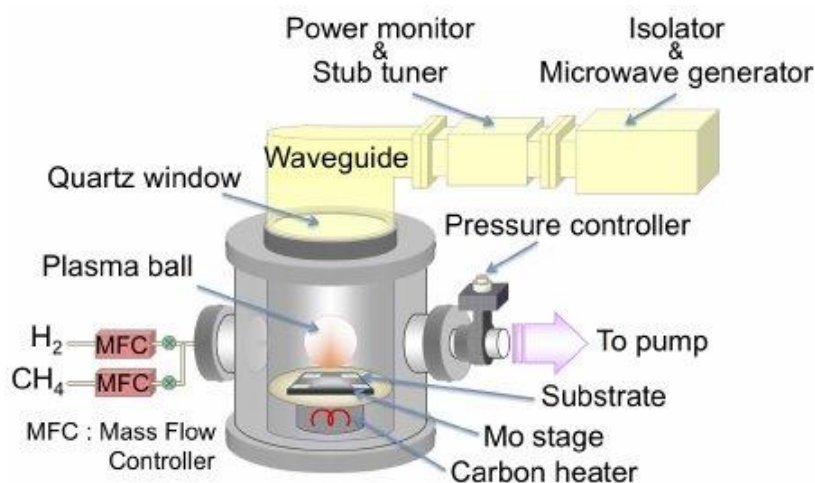


Figure 4. Schematic diagram of an ASTeX-type MW PE-CVD reactor used for nanocrystalline diamond thin film and carbon nanotube growth.^[53]

The substrate temperature can be controlled by the carbon heater beneath the molybdenum stage. The pressure of the chamber was between ≈ 10 -80 Torr, and the plasma ball size increases as microwave frequency increases or chamber pressure decreases.

The absence of electrodes in a MW PE-CVD system is advantageous in preventing contamination of the diamond during growth by graphitic deposits, which can build-up on electrodes.^[54] The disadvantage of using a MW PE-CVD system for diamond growth is that the pressure and microwave frequency cannot be controlled separately, as the two parameters depend on one another.^[53]

1.3.3 Pulsed DC Plasma Enhanced CVD (PDC PE-CVD)

PDC PE-CVD has been used for the growth of polycrystalline^[38,55] and nanocrystalline^[56] diamond thin films, and has been widely reported for diamond-like carbon growth.^[57-59] The advantage of PDC PE-CVD compared to MW PE-CVD is that there is more control over the growth parameters, such as the power input, pressure and pulse frequency. The diamond growth area can also be adjusted by the size of the substrate and the interelectrode separation.^[60] **Figure 5** shows a schematic diagram of a PDC PE-CVD reactor.

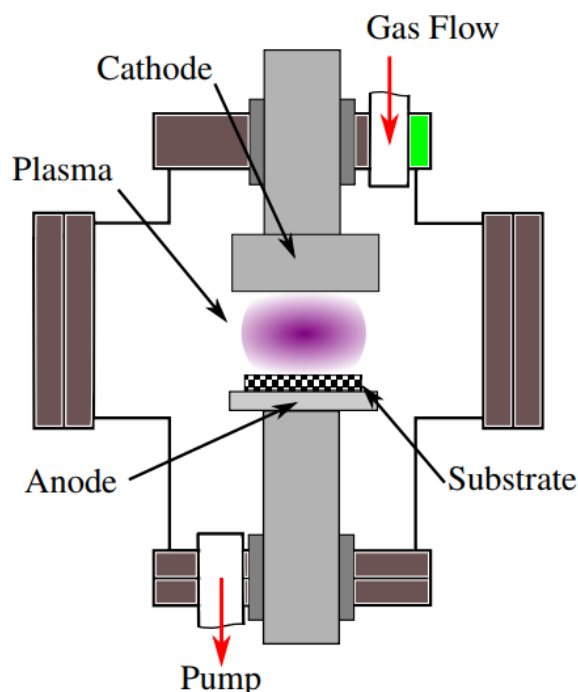


Figure 5. Schematic diagram of a PDC PE-CVD reactor set-up.^[61]

A pulsed DC power supply is applied to two electrodes, the cathode and anode (ground electrode), which are connected in parallel. A Townsend discharge is initiated by photoemission of the cathode or photoionization of the gas by background radiation, in which electrons are accelerated from the cathode toward the anode. Electron impact ionization of the gas species between the electrodes occurs, which initiates an electron avalanche. Positively charged ions that are created are also accelerated by the electric field towards the cathode, and upon striking the electrode, secondary electron emission can occur by the Auger effect. These secondary electrons can then cause more electron avalanches by

electron impact ionization, further activating the gas species for diamond deposition onto the substrate, which is positioned upon the anode.^[62–64] The substrate temperature can be controlled by adjusting the water flow to the cooling system of the electrodes.

The breakdown voltage (V_B) is the voltage necessary to initiate a discharge between two parallel electrodes,^[65] and is dependent primarily on the pressure of the system (p) and the electrode separation (d). This relationship is given by Paschen's law (**Equation (2)**),^[66] in which A and B are constants, and γ_{SE} is the secondary electron emission coefficient.

$$V_B = \frac{Bpd}{\ln(Apd) - \ln\left[\ln\left(1 + \frac{1}{\gamma_{SE}}\right)\right]} \quad (2)$$

The pulsing mode of the power supply has been shown to improve growth conditions by reducing the possibility of arcing between the electrodes and the substrate or chamber walls, and therefore helps to maintain a stable plasma. Furthermore, higher charged particle densities can be achieved at the same power compared to non-pulsed discharges, which allows for better growth rates with less damage to the electrodes.^[67–69] The reverse time can be defined as the time at which power is switched off to the plasma in-between pulses.^[70]

1.4 Optimisation: The Taguchi method

One of the simplest methods of optimisation, known as the one-factor-at-a-time method,^[71] involves changing each variable individually whilst keeping all others constant and observing the effect on the process. For cases where there are more than two parameters to consider with non-linear behaviour, such as those involved in CVD, trying to optimise the system would require a multitude of experiments which renders the approach impractical. An alternative method employs orthogonal arrays to test two or more independent variables at once, each at predefined level values. This acts to minimise the number of experiments required to optimise the system, reducing the time and cost of the optimisation. Designed by Genichi Taguchi in the 1950s,^[72] this statistical technique is used to improve efficiency, quality, cost, and performance of a process by reducing variation from noise parameters.^[73] The method is based upon the work on design of experiments by R. A. Fisher,^[74,75] and assumes that the performance of an independent variable at a specific level value does not rely on the level settings of the different variables, i.e. interaction effects are negligible. **Figure 6** shows a flowchart of the method.

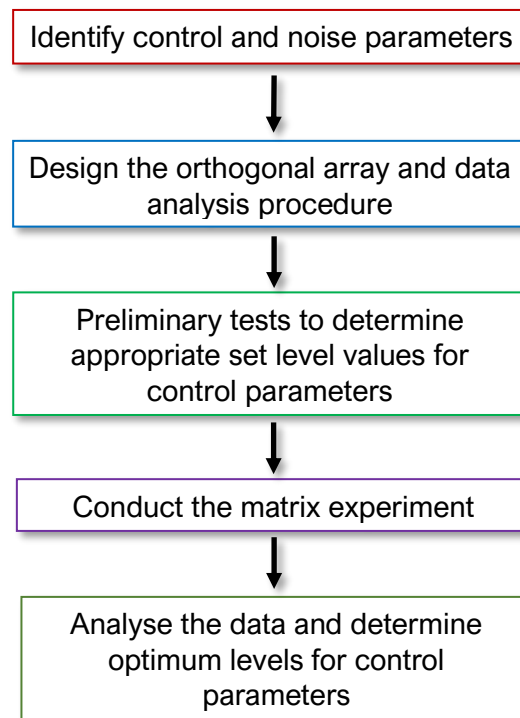


Figure 6. Flowchart of the Taguchi method. Adapted from reference ^[73].

Parameters which influence the performance of the process can be separated into three categories: noise, signal and control.^[76] Noise parameters, defined as either uncontrollable external parameters or parameters too costly and difficult to control, are considered the main source of variation in the process. The signal parameters are input parameters which communicate the desired outcome from the system. The control parameters are the independent variables which are chosen to be set at predefined level values. The method aims to maximise the signal-to-noise ratio in order to minimise the variation in the control parameters in response to the noise parameters, and to maximise the variation with respect to the signal parameters.

To illustrate this, **Table 2** shows the experiment design of 4 independent variables, labelled as control parameters A, B, C and D, at 3 different level values. Due to the counterbalance property intrinsic to an orthogonal array, evenly-spaced level values chosen for the control parameters are non-essential.^[77] The orthogonal array results in a total of 9 experiments required to optimise the process. If the one-factor-at-a-time method was used for the optimisation of 4 control parameters at 3 different levels, 64 experiments would be required. Therefore, by using the Taguchi method for optimisation, time and resources are saved.

Table 2. L₉ (3⁴) orthogonal array: 9 tests, 4 control parameters, 3 levels.^[78]

Experiment Number	Control Parameter			
	A	B	C	D
1	1	1	1	1
2	1	2	2	2
3	1	3	3	3
4	2	1	2	3
5	2	2	3	1
6	2	3	1	2
7	3	1	3	2
8	3	2	1	3
9	3	3	2	1

The method has been used to optimise numerous CVD diamond-growth processes, such as PE-CVD,^[79] inductively-coupled PE-CVD,^[80] Hot Filament (HF)-CVD^[81] and time-modulated CVD.^[82] The optimisation of a PDC PE-CVD reactor by the Taguchi method has not been formally reported on as of yet, however research has been carried out in the Bristol Diamond Lab^[83–85] which this project aims to follow on from, highlighting the novelty of the research reported herein.

1.5 Techniques for characterisation of CVD diamond thin films and growth analysis

1.5.1 Raman and Infrared (IR) spectroscopy

Raman spectroscopy is a qualitative and quantitative technique which relies upon scattering of light induced by a change in polarizability between two or more bonded atoms, to detect the vibrational modes of a molecule or structure. Photons from monochromatic light in the UV/VIS region excite electrons into virtual energy states. As these states are forbidden, and are thus unstable and short-lived, strong laser light is necessary to increase the promotion of electrons into these states, in order to detect a strong enough emission of scattered light upon fast relaxation of the electron to a lower-energy level. This can be visualised by the energy level diagram shown by **Figure 7**. Most of the scattering is elastic, known as Rayleigh scattering, in which the energy emitted upon relaxation is the same as the energy of the incident photon. The remaining scattered light is inelastic, known as Raman scattering, which can occur in two ways: the energy emitted is less than that of the incident photon (Stokes Raman scattering), or the energy emitted is more than that of the incident photon (Anti-Stokes Raman scattering).

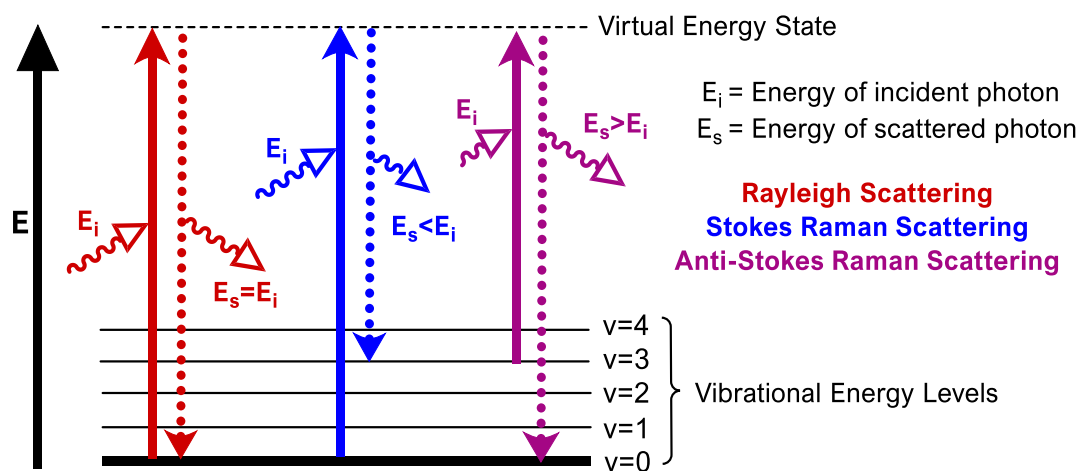


Figure 7. Energy level diagram showing the different types of scattering that can occur. Information sourced from reference ^[86].

The scattered light is directed by lenses through a monochromator and the Rayleigh scattering is filtered out. The resulting light is detected by a CCD detector, processed and the structure of the sample can be identified by the characteristic absorbance peak pattern projected as a spectrum on the computer. This technique offers a quick and simple method to assess the quality of the diamond grown. Impurities such as trans-polyacetylene and several forms of amorphous carbon (including graphite) can be detected by difference in hybridisation of the carbon atoms in the structures. Diamond exhibits a characteristic sharp peak at a Raman shift of 1332 cm^{-1} by green laser light (532 nm), which arises from the theoretically identical sp^3 hybridised carbon-carbon bonds in the lattice. On the other hand, as an example of carbon impurity, the bonding between carbon atoms in graphite layers is sp^2 hybridised. This is a stronger bond than between carbon atoms in diamond (see section 1.1 for bond energies) and thus the vibrational bond frequency is higher and hence a peak arises at a higher Raman shift between $1500\text{-}1600\text{ cm}^{-1}$.^[87] This peak is broader than the diamond peak due to the additional scattering of light from many defects in the graphite structure, as opposed to the sparse number of defects in high quality diamond. The relative intensity of the Raman peaks is proportional to the concentration of different structures and compounds in the sample.

IR spectroscopy relies on the absorption of light induced by a change in permanent dipole moment between two or more bonded atoms in a structure. The absorbed light lies in the infrared region of the electromagnetic spectrum, which corresponds to distinct transitions between vibrational energy-levels in an electronic energy state, induced by a vibration of a polarised bond. It is for this reason that IR spectroscopy can be useful in detecting non-carbon impurities in a diamond lattice, as the bond between carbon and the non-carbon atom in the impurity would possess a dipole moment.

Both spectroscopic techniques have been used to give information about the isotopic content of diamond.^[12,88] As shown by the IR spectrum in **Figure 8 (a)**, natural and CVD diamond exhibit intrinsic two-phonon and three-phonon bands between 1800-2700 cm^{-1} and 2700-4000 cm^{-1} , respectively. The purity of diamond can be assessed by absorption lying between 1000 cm^{-1} and 1800 cm^{-1} , which would appear if nitrogen or boron were present as impurities. As the ^{13}C content of diamond increases, the absorption bands appear at lower frequency due to the inverse cubed-root relationship of reduced mass with frequency. This effect can also be observed in Raman spectroscopy (**Figure 8 (b)**). In 1990, Chu *et al.* reported that by varying the isotopic composition of diamond grown by HF-CVD, the Raman peak at 1332 cm^{-1} characteristic to natural diamond was found to have shifted to 1282 cm^{-1} for ^{13}C diamond.^[34] Their work also showed a linear relationship between the Raman peak frequency shift and the ^{13}C mole fraction for mixed-isotope films.

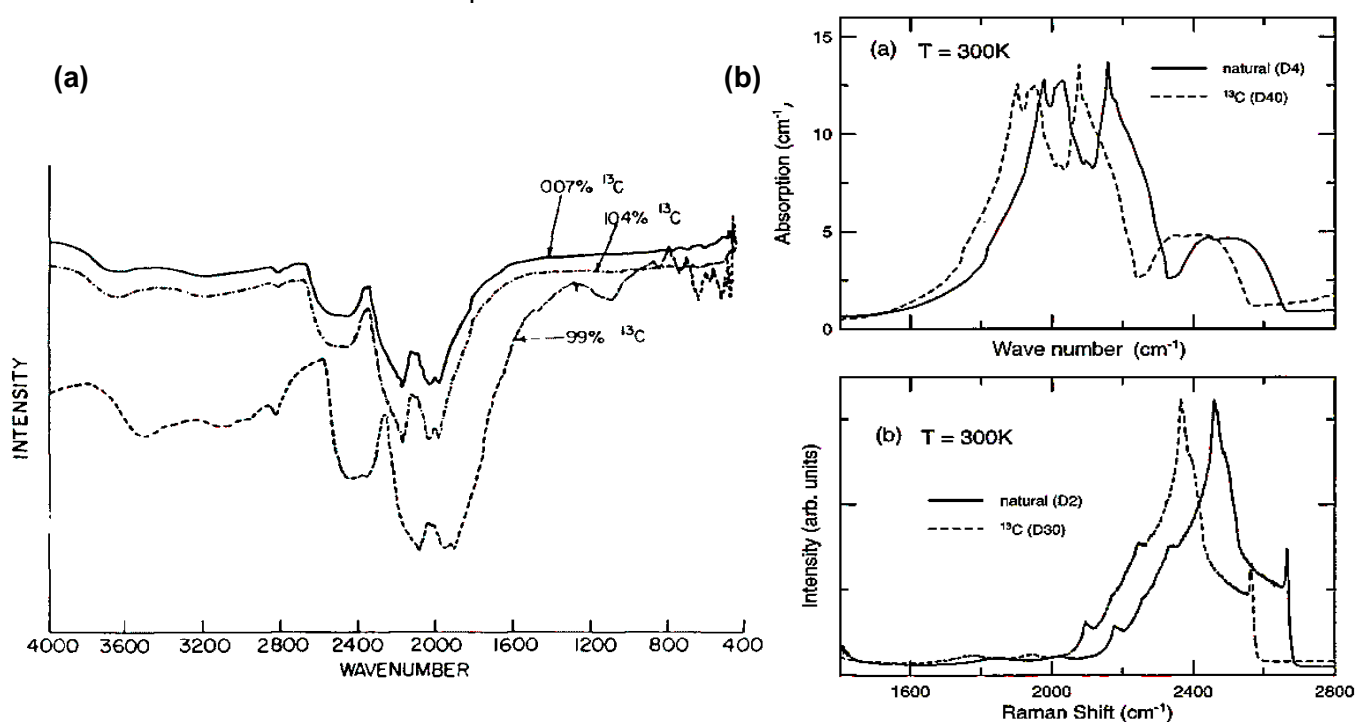


Figure 8. (a) IR spectrum of diamond with varying ^{13}C isotopic content.^[12] **(b)** IR spectrum (top) and Raman spectrum (bottom) of natural and ^{13}C diamond.^[88]

1.5.2 Scanning Electron Microscopy (SEM) and Transmission Electron Microscopy (TEM)

SEM uses a beam of focused electrons to create an image of the surface of a solid sample. **Figure 9** shows a schematic diagram of the SEM apparatus.

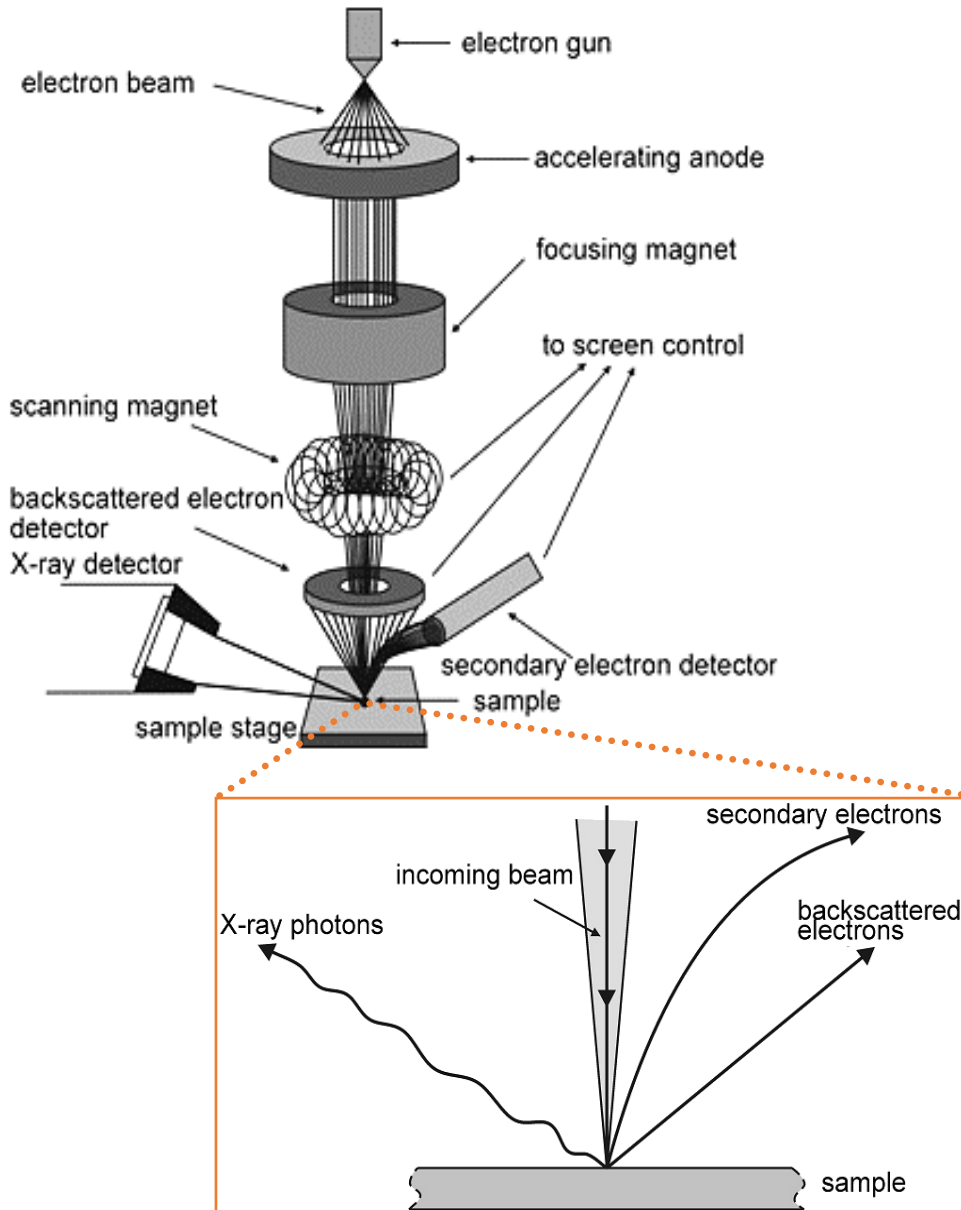


Figure 9. Schematic diagram of a scanning electron microscope. Edited from reference ^[89].

The electron beam is accelerated down the column by magnets to focus onto the sample. These accelerated electrons will ionise the surface atoms, which inelastically scatter the absorbed energy, emitting low-energy secondary electrons. These are detected and can be used to decipher information about the surface topography, with a maximum resolution of 1-2 nm.^[90] Alternatively, the electron beam can penetrate deeper atomic layers, generating X-ray emission, which can provide elemental analysis of the sample. Another potential outcome is the back-scattering of the electrons off the surface atoms by inelastic scattering, which can contribute to achieving a deeper profile of the sample surface. Furthermore, backscattering electrons have a 'Z-contrast' effect, in which the larger the atomic number of a species, the more backscattering electrons it will yield, resulting in a brighter area. This can provide

more information on the elemental composition of the surface atoms. Finally, an image is created pixel-by-pixel as the beam rasters over the sample. This is achieved by a scintillator on the detector which converts secondary electrons into light, and a photodiode which converts this light into a voltage. This voltage corresponds to a certain brightness which will appear as a pixel on a computer screen.

SEM is an important tool used to visualise the different morphologies of the growth which can indicate the quality of the diamond and the conditions of the growth. **Figure 10** shows a series of SEM images of diamond films grown by MW PE-CVD to demonstrate the effects of gas pressure on the morphology and growth rate of diamond films.^[91]

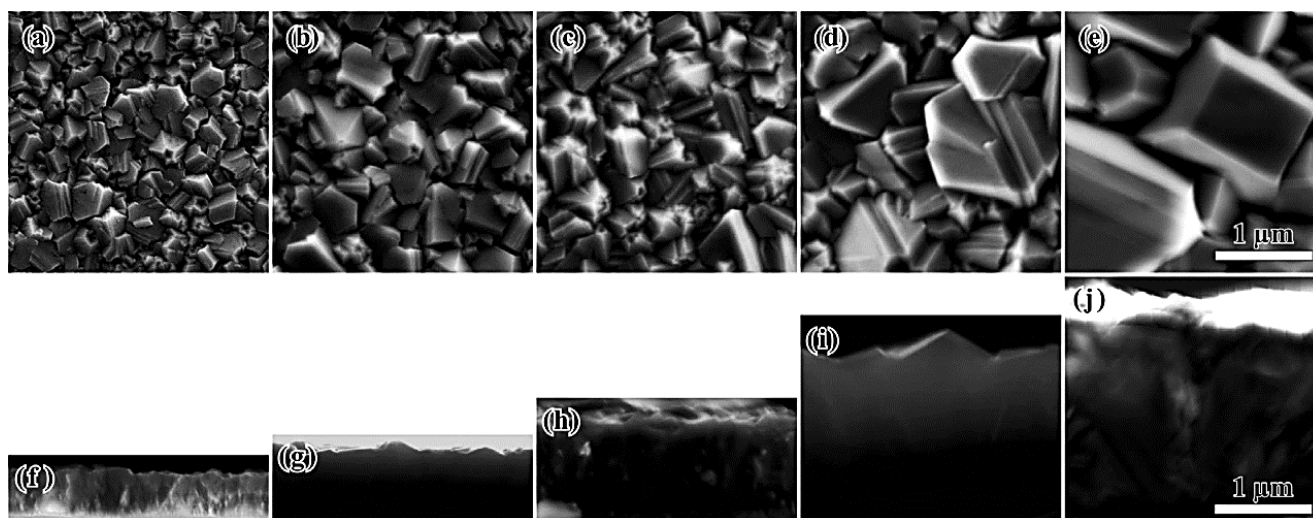


Figure 10. SEM images of diamond films grown using 6 kW, 3% CH₄ and varying pressures. Images (a)-(e) show top surface of films, (f)-(j) show corresponding cross-sectional view of films. Pressures: (a) and (f) 40 mbar, (b) and (g) 50 mbar, (c) and (h) 60 mbar, (d) and (i) 80 mbar, (e) and (j) 90 mbar.^[91]

In a similar way to SEM, TEM can be used to visualise the structure of the sample, but instead relies on transmitted (not scattered) electrons from atoms at the surface and in the bulk of the sample. This means TEM can provide information on the internal composition of the sample, to detect grain boundaries and defects. This can be visualised by **Figure 11 (1)**, which shows a series of micrographs of nanocrystalline MW PE-CVD diamond films, grown under an increasing H₂/Ar ratio gas composition with a constant CH₄ concentration.^[92] The black and white regions of the micrographs show the different grain boundaries in the structure, which become more dense and larger as the H₂ concentration increases. **Figure 11 (2)** shows a magnified grain boundary of a diamond thin film, which confirms the presence of (111) planar defects by the electron diffraction and Fourier-transformed diffractogram.

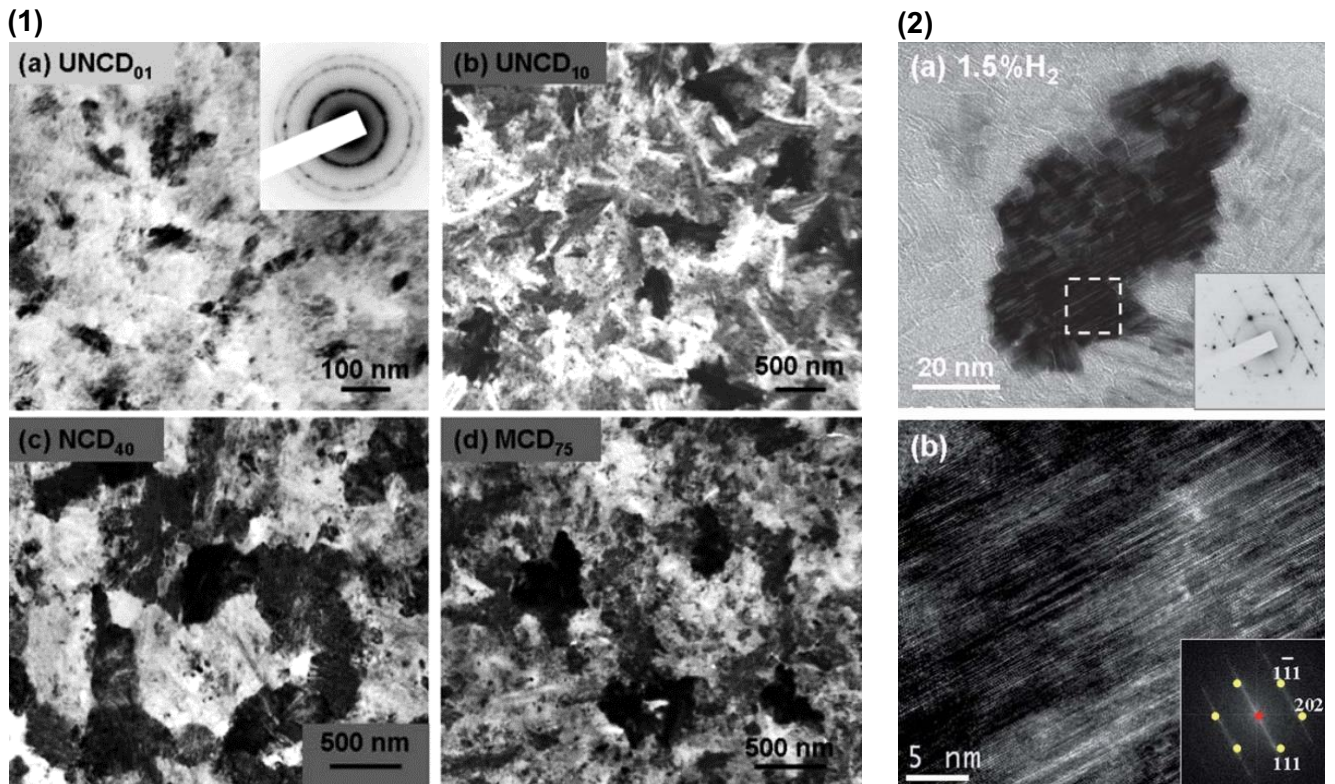


Figure 11. (1) TEM micrographs of diamond films grown in an Ar/H₂ gas mix with varying x% [H₂]. (a) x = 0, (b) x = 10, (c) x = 40, (d) x = 75. **(2)** TEM micrographs for the diamond films grown in Ar/H₂ gas mix with 1.5% [H₂]. (a) Bright field image and inset electron diffraction pattern, (b) the structure of the region designated in (a) and corresponding inset Fourier-transformed diffractogram.^[92]

1.5.3 Optical Emission Spectroscopy (OES)

This technique is used to provide details of the elemental content of a solid, liquid or gas. OES works by detecting UV-VIS radiation emitted from thermally excited species in a plasma.^[93–96] The emission occurs by the relaxation of excited electrons in higher-energy levels to lower-energy levels in the species. Initially the electrons are promoted to higher levels by collisions between the reactive species and other species or electrons within the plasma. The transitions are well-defined and produce a characteristic spectral emission, consisting of narrow atomic spectral lines corresponding to a particular atomic species. **Table 3** shows the various species in a H₂/CH₄ gas mixture and their corresponding electronic transitions and peak wavelengths.^[97]

Table 3. Optical emission lines for species in a H₂/CH₄ gas mixture.^[97]

Species	Transition	Peak position (nm)
H _α	n' = 3 → n = 2	656.1
H _β	n' = 4 → n = 2	486.1
H _γ	n' = 5 → n = 2	434.1
H _δ	n' = 6 → n = 2	410.0
H ₂	G ¹ Σ _g ⁺ → B ¹ Σ _u ⁺	462.9
CH	B ² Δ → X ² Π	387.0
	A ² Δ → X ² Π	431.5
CH ⁺	A ¹ Π → X ¹ Σ	422.2
	A ¹ Π → X ¹ Σ	417.1
C ₂	d ³ Π _g → a ³ Π _u	516.3
CN	B ² Σ → X ² Σ	388.3

OES offers an easy, non-invasive method to study the processes occurring in the plasma during diamond growth in plasma enhanced CVD reactors. For example, **Figure 12** shows emission spectra from a study of a microwave activated CH₄/Ar/H₂ plasma for diamond CVD growth.^[98] Actinometry was used in this study (and in many others),^[99–102] to determine the relative concentrations of H (*n* = 1) radicals in the plasma. The process essentially relies on comparing the emission intensity of ground state species with those of electronically excited state species.

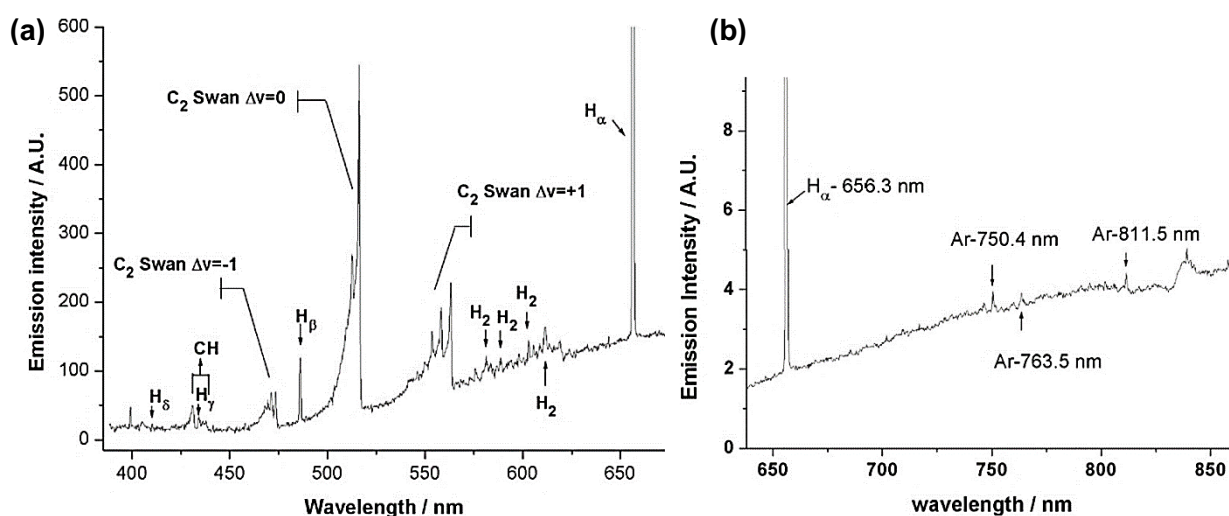


Figure 12. (a) OES measured in wavelength range 390–670 nm, emission from electronic excited H atoms and to C₂(d) and CH(A) radicals shown. (b) OES measured in wavelength range 640–860 nm, emission from H (*n* = 3) and Ar (4*p*) atoms shown.^[98]

As would be expected, rotational and vibrational transitions arising from an electronic excited state of a species are affected by its mass. It has been shown that the rotational and vibrational frequency of the excited ¹³CH species from a ¹³CH₄ feedstock in the plasma is higher than that of CH from a natural CH₄ feedstock, resulting in a shift in the OES.^[103]

1.5.4 Nano-scale Electron Spectroscopy for Chemical Analysis (NanoESCA)

The Bristol NanoESCA facility^[104] is a specialised and highly sensitive surface analysis instrument, capable of chemical state mapping. The characterisation methods built into the NanoESCA which will be described, offer powerful tools to probe the surface chemistry of CVD diamond.^[105,106]

PhotoEmission Electron Microscopy (PEEM) is a technique which offers real-time spatially resolved spectroscopy and topography imaging of a sample. This is achieved by collecting secondary electrons emitted from the surface atoms of a sample exposed to X-ray or UV radiation. These electrons are accelerated by an electric field towards a channel plate which acts to multiply the intensity of the emission and can provide spatial resolution. The electron pattern can be imaged by a CCD sensor or fluorescent screen, providing impressive lateral resolution of 13 nm, and a variable image field view ranging from 3 μm to 1100 μm .^[104] This type of microscopy differs from SEM and TEM by sampling the entire area of the surface at once and not by scanning over the surface. This means the sample undergoes uniform exposure to radiation, reducing any damage which could occur to sensitive surfaces by the high-energy beam of electrons from a scanning probe.^[107] For example, energy-filtered PEEM has been used to create work function maps of semiconducting lithium-oxygen terminated diamond films, to assess the low work function coverage. This would correspond to a low negative electron affinity, a key property for effective low temperature thermionic energy converters.^[105]

Micron-scale angle-resolved photoemission spectroscopy can be used to visualise the momentum-resolved electronic structure of the surface layers of a sample, which provides useful information on the electronic and optical properties of the material.^[108] The spectroscopic technique images in real and reciprocal space to determine band structure of the material, using energy-filtered PEEM to measure the kinetic energy of photoelectrons from the sample. This technique was used to follow the valence band maxima of (100) and (111) diamond surfaces throughout change in termination from hydrogen to oxygen.^[106]

Spot Profile Analysis Low Energy Electron Diffraction (SPA-LEED) is a technique used to visualise the surface morphology of a sample in reciprocal space. A diffraction pattern is formed by the interference of the diffracted low energy collimated electrons passed through the crystal structure of the sample. The emerging electrons are detected, counted and projected by an electron multiplier through an aperture onto a fluorescent screen, which shows the atomic positions in the crystal as spots (in reciprocal space). The spot intensity and shape is dependent on the presence of defects, areas of strain or dislocations which can be highlighted by spot broadening or splitting.^[109] SPA-LEED could be used to further study the effect of ^{13}C isotope content in diamond on the lattice constant, which has been shown to decrease with increasing ^{13}C content.^[4]

High-resolution X-ray Photoelectron Spectroscopy (XPS) is a technique which can determine elemental composition of a sample, capable of real time analysis and mapping. X-rays are fired at the surface

atoms and the kinetic energies of the resultant photoelectrons are measured to produce a spectrum.^[110] One of the first studies to follow the nucleation and growth of diamond *in situ* by XPS was by Belton *et al.* in 1989,^[111] and since then the technique has been used widely to track surface chemistry of diamond.^[106,112,113]

1.6 Project aims

Over the past three years, several research projects by members of the Bristol University Diamond Group have been focused on constructing and optimising the reactor in order to achieve the best growth rates and quality of diamond thin films.^[83–85] Most recently, Helen Harris optimised the reactor to grow diamond thin films from a CH₄/Ar/H₂ gas mixture. The fastest growth rate achieved was 49.8 μm h⁻¹, which is high compared to diamond growth using DC PE-CVD reactors from the literature (see **Table 4**). The growth runs were limited to a power of 2.5 kW due to the efficiency of the water-cooling system. In order to prevent overheating and damage to the structural integrity of the pipes, the maximum water flow output temperature from the cathode and ground electrode was 40°C. The power was sufficient enough to dissociate the methane molecules into radicals, however due to the limited cooling of the ground electrode, the temperature of the substrate was too high for stable diamond growth.

Table 4. Diamond growth conditions by DC PE-CVD systems.

Power (kW)	Growth Rate (μm h ⁻¹)	Methane conc. (%)	Pressure (Torr)	Substrate area (cm ²)	Reference
2.5	49.8	5.6	200	7	85
40	11	6	150	78.5	114
3.7	54	6	200	1	55
75	7-9	7	100	324	115
4	20	2	200	≤ 0.8	116

The next logical step to take with regards to the design of the reactor was to improve the water-cooling system so that higher powered, more stable plasmas could be attained, and consequently the effect of input power on diamond growth rate and quality could be assessed in further detail using PDC PE-CVD. Therefore, the project reported herein aimed to determine the optimal conditions to grow diamond at a high rate and to a high quality using a CH₄/Ar/H₂ gas mixture, following the installation of a copper water-cooling jacket to the ground electrode. Owing to nearly an eight-fold increase in the thermal conductivity of copper compared to steel (385.0 W m⁻¹ K⁻¹ and 50.2 W m⁻¹ K⁻¹, respectively),^[117] copper had been chosen as a suitable material to replace the stainless steel parts for the water-cooling jacket to improve the efficiency of the heat dissipation from the substrate. The optimisation and growth were conducted in a PDC PE-CVD reactor, held in the CVD Diamond Lab at the University of Bristol.

A comparison of growth conditions by DC PE-CVD systems (see **Table 4**) showed that powers of 2.5-4 kW have shown higher growth rates than those ≥ 40 kW, so the new system optimised in this

project worked towards reaching ≈ 4 kW of power. However, it is known that pressure, methane concentration and substrate area also play a major role in diamond growth, so it is certain that the growth rate is not dependent on the power alone. Therefore, it was important to consider these factors in the optimisation.

In order to optimise the new reactor set-up, the Taguchi method was applied to determine the best combination of five control parameters: pressure, power, pulse frequency, methane concentration and argon concentration. Possible control parameters that could have been tested if it weren't for the time constraints of the project, were the electrode separation, substrate size, total mass flow, water flow to the electrodes and the substrate temperature. The temperature of the substrate is integral to diamond growth, so this would have been an informative parameter to control. However, as water flow to the electrodes, substrate temperature, and input power are all dependent on one another, only one parameter could have been controlled. In this case the power was controlled, leaving the remaining two parameters to be considered as noise. A pyrometer was not available for use, so substrate temperature could not have been measured. Furthermore, keeping water flow consistent throughout a growth run would have been impractical to do during this initial optimisation of the reactor, which is one of the reasons why it was not chosen as a control parameter. This was due to the threat of damaging the structural integrity of the water pipes if the water output reached temperatures $\geq 40^\circ\text{C}$, which would have been high risk due to the number of unknowns associated with growth using such a new reactor set-up.

Methane was chosen as the carbon-containing feedstock gas for several reasons. Firstly, it has been widely reported on as a carbon feedstock for CVD diamond growth, so this was useful for the purpose of comparing the results of this project to the literature. Secondly, it is an abundant, cheap and relatively non-toxic (in low doses)^[122] feedstock gas to use. As methane is a gas at room temperature it can be easily introduced into the reactor chamber. Finally, in order to minimise lattice defects, it is important that only single carbon species are added to the surface radical sites on the forming diamond lattice, which is most probable by using methane.

Argon was chosen as a dilution gas in addition to hydrogen as a means of increasing the diamond growth rate, by promoting hydrogen dissociation into H radicals in the plasma (see section 1.3.3). The effect of argon on the quality of diamond is less clear, and can be assessed by analysing the diamond and amorphous carbon peak intensities in Raman spectra. Generally, the higher the amorphous carbon peak intensity, the poorer the diamond quality. Zhu *et al.* reported that by increasing argon concentration up to 35%, the amorphous carbon formation remains consistent,^[44] and in agreement, Shih *et al.* reported that the best quality of diamond was achieved at 50% argon concentration.^[123] However, the results by Tallaire *et al.* contradict this, showing that amorphous carbon formation increases steadily upon increasing Ar concentration from 0-40%.^[40] Evidently, the effect of argon on

diamond quality has not been well established, so the project aimed to gain further insight into this relationship.

As highlighted in section 1.2, isotopically pure ^{13}C diamond has one such use as a material in beta-voltaic batteries. Considering this, another aim for this project was to optimise the system for closed cycle growth, with the purpose of identifying the minimum concentration of $^{13}\text{CH}_4$ feedstock gas necessary to grow high quality ^{13}C diamond thin films. The closed cycle conditions act to reduce waste and save money, as a $^{13}\text{CH}_4$ gas feedstock is expensive (240 £ L^{-1} [124]) compared to natural CH_4 gas (2.80 £ L^{-1} [125]), which are important factors to consider if the reactor were to be commercialised for larger-scale growth of ^{13}C diamond.

Chapter 2: Methodology

2.1 The PDC PE-CVD reactor set-up

A 15 kg copper water-cooling jacket with a limiting water outflow area of $\approx 380 \text{ mm}^2$ was installed in the reactor, encasing the ground electrode.² Post installation, the chamber was subjected to a 48 hour vacuum pump-down, in which the pressure reached $\approx 15 \text{ mTorr}$. The vacuum of the system was tested by stopping the vacuum pump and recording the pressure climb over 5 minutes. Preliminary growth runs were conducted to gauge a range of values for the growth conditions, to strike a stable plasma, and to tune the water-cooling input and output flow rates from the cathode and ground electrode to reach a safe water/pipe temperature ($\leq 40^\circ\text{C}$). **Figure 13** shows a schematic diagram of the modified reactor set-up.

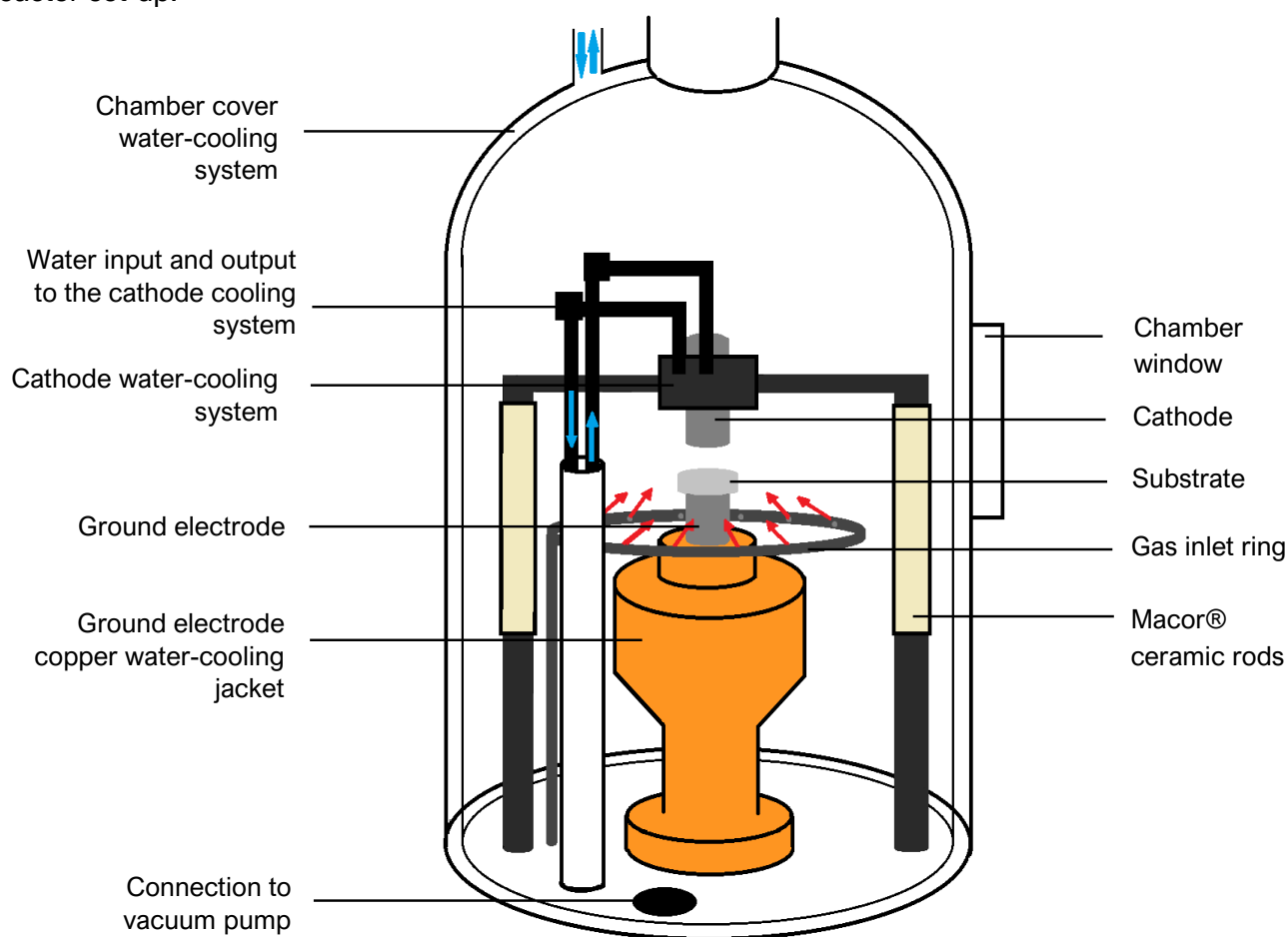


Figure 13. Schematic diagram of the modified reactor set-up with the new ground electrode water cooling jacket. The blue and red arrows indicate water and gas flow, respectively.

The tungsten substrates had a surface area of 7.8 cm^2 for growth, with a diameter of 3.15 cm and a thickness of 0.3 cm . Each electrode had a diameter of 2.5 cm , the inter-electrode separation between the tungsten cathode and ground electrode was 0.15 cm , and the height of the electrodes were 9.4 cm and 5.8 cm , respectively. The steel gas inlet ring contained 18 evenly spread apertures (with diameters

² See appendix for more detailed diagrams of the water-cooling jacket design, created by Dominic Palubiski (**Figure 32**).

of 0.05 cm) to direct the gas uniformly toward the electrode gap. The Macor® ceramic rods functioned to insulate the live electrode (cathode) from the grounding and to act as a structural spacer of the electrodes. The reactor operated an Advanced Energy® Pinnacle® Plus+ 10 kW Pulsed-DC power supply, which runs an arc suppression system and has a voltage limit of 650 V. The growth parameters were controlled by a Delphi computer program written in-house, which displayed the temperature of the water from the substrate and cathode, and the pressure of the chamber. The program allowed for control over the opening and closing of the mass flow controllers. The desired set-point values for the pressure and gas flow rates required manual entry into the program, and the power, pulse frequency and reverse time were set by pressing the buttons and adjusting the dial on the control panel at the front of the instrument.³ The stainless steel chamber cover (height: 45 cm, diameter: 32 cm) operated by hydraulic action, allowing for easy lifting and lowering of the cover.

2.2 Taguchi optimisation

2.2.1 Design of the orthogonal array

An L16' 4⁵ orthogonal array consisting of 16 experiments⁴ was designed with 5 control parameters set at 4 different levels (see **Table 5**). The appropriate set level values for each control parameter were determined by the preliminary growth runs conducted post water-cooling jacket installation. The set reverse times corresponding to the pulse frequency set level values are detailed by **Table 9** in the appendix.

Table 5. Control parameter set-level values for the Taguchi optimisation.

Set level	Pressure (Torr)	Power (kW)	Pulse Frequency (kHz)	Argon flow rate (sccm*)	CH ₄ flow rate (sccm*)
1	130	3.70	75	0	5
2	175	3.85	100	5	10
3	200	4.00	125	10	15
4	225	4.15	150	20	20

* standard cubic centimetre per minute.

2.2.2 Cleaning and growth runs

The following steps were taken for the cleaning and growth runs:

1. The substrate was first cleaned by water and sand paper, dried, and placed on top of the ground electrode in the chamber.
2. The chamber was evacuated (dial on power control panel to 'OPEN', with switch up) for ≈ 16 hours to reach a pressure of 15 mTorr.

³ Labelled images of the computer system and control panel are located in the appendix (**Figure 33** and **Figure 34**).

⁴ The full conditions for the 16 Taguchi growth runs are detailed in the appendix (**Table 10**).

3. The reactor was prepared for a hydrogen cleaning run, to ensure a thorough clean of the substrate.
 - i) The pressure (180 Torr), hydrogen flow rate (500 sccm), pulse frequency (125 kHz), and reverse time (2.6 μ s) set-point values were inputted into the system.
 - ii) The gas flow valve was opened, and the chamber pressure stabilized at 1.8 Torr.
 - iii) The plasma was struck at 50 W, and the vacuum pump was closed as the dial on the power control panel was turned to 'EXT'. The power was incrementally increased by 250 W for every 10 Torr increase in pressure, until the pressure set-point and a power of 3.5 kW were reached.
 - iv) After 1 hour, the power was turned off and the system was evacuated for \geq 30 mins to allow for the system to cool.
4. The growth run was set-up and conducted in the same way as the cleaning run.
 - i) If argon was included in the gas mixture, it was introduced into the reactor with the hydrogen at the start of the run.
 - ii) Methane was introduced once the pressure of the system reached 100 Torr.
 - iii) After 1 hour of growth, measured as 1 hour after the set-point values for the control parameters were reached, the power was turned off and the gas mass flow controllers were closed.
 - iv) To open the chamber, the dial on the power control panel was set to 'CLOSE', and argon was pumped into the system (bypassing the mass flow controllers) until \approx 760 Torr was reached. The chamber cover was lifted, and the substrate removed for analysis.
5. Steps 1-4 were repeated for the 16 Taguchi growth runs. Once the optimised conditions for growth rate and quality were determined, a 1 hour trial run and a 3 hour growth run were conducted for both sets of conditions, following steps 1-4. The purpose of the 1 hour trial run was to test the optimised conditions to see if the plasma was stable to perform the longer 3 hour run.

2.3 Characterisation

The growth distribution and quality from the Taguchi runs and optimised growth runs were assessed by recording 13 Raman spectra across every substrate. The spectra were recorded with the in-lab Renishaw® Raman Spectrometer equipped with a Leica® Optical Microscope, using green laser light (532 nm).

The growth rate and quality of growth from the Taguchi runs and optimised runs were visualised by a Jeol® JSM-IT300LV Scanning Electron Microscope, which was used to image the variation and coverage in growth.

An Ocean Optics® USB2000+UV-VIS-ES Optical Emission Spectrometer was used to measure the elemental content of the plasma during the 3 hour optimised growth runs for quality and growth rate.

Chapter 3: Results and Discussion

3.1 Installation of the ground electrode water-cooling jacket and modifications to the reactor

Figure 14 shows the ground electrode set-up before and after installation of the copper water-cooling jacket. The steel water-cooling jacket had a water outflow area of 32 mm² which limited the flow to the whole cooling system. Prior to installation, the substrate and ground electrode would glow at a power of 2.5 kW. By increasing the water outflow area, the efficiency of the cooling system increased significantly, such that at higher power (4 kW) the ground electrode would not glow and the substrate would have a dull glow (see **Figure 15**). The leak rate was calculated to be 0.06 mTorr min⁻¹ which was sufficiently low enough to be deemed to have a negligible effect on any growth runs.

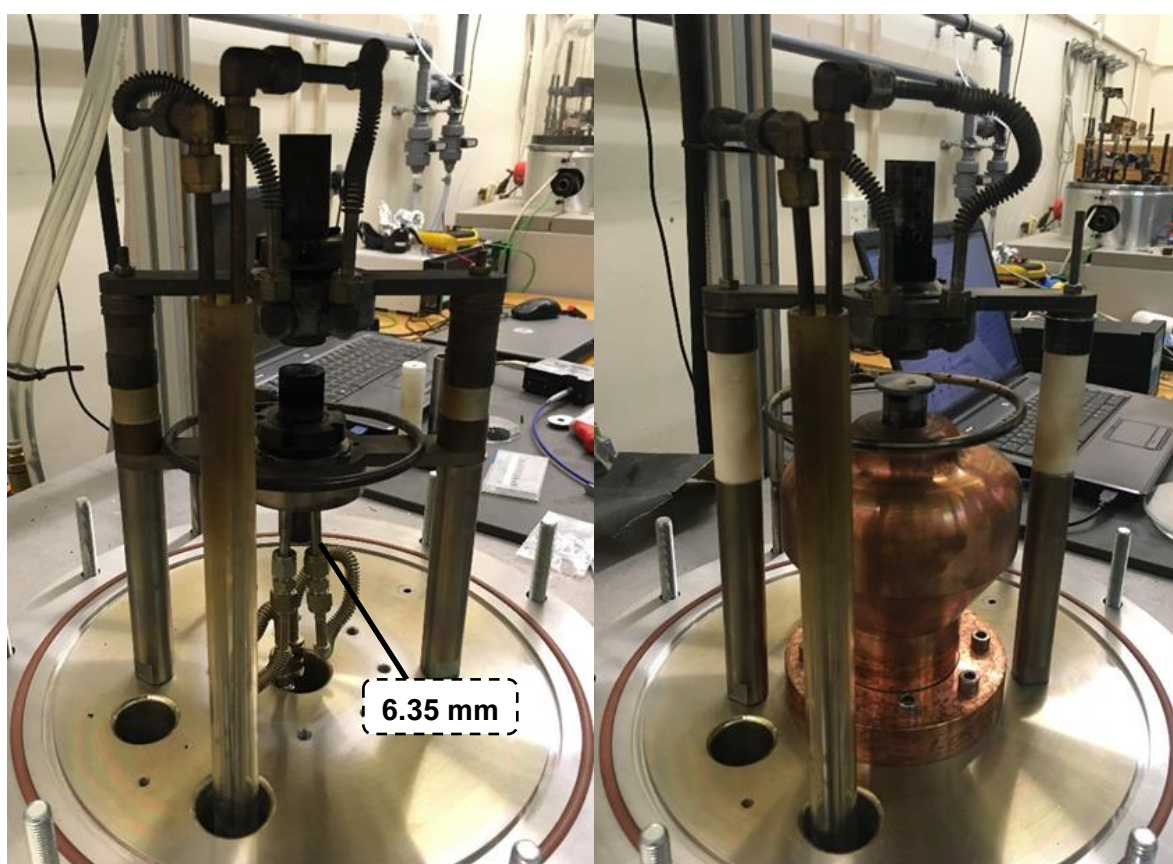


Figure 14. Before (left image) and after (right image) the installation of the new copper water-cooling jacket to the ground electrode.

From observations during the preliminary growth runs, the electrode separation and the rate of water flow to the different parts of the reactor were adjusted accordingly to achieve a stable plasma at high powers (≈ 4 kW), without overheating of the water-cooling system. Initially, the electrode separation was 18 mm, however when the power reached 3 kW and the pressure reached 225 Torr, arcing of the plasma caused an increase in voltage over the limit of 650 V, which tripped the power. To amend this, the electrode separation was reduced to 15 mm which allowed for the relatively high-pressure

conditions whilst maintaining a low breakdown voltage, and hence a low current density (refer to **Equation (2)**, section 1.3.3). This meant that a power of 4.15 kW and pressure of 230 Torr could be reached without tripping the power. It was important that the electrode separation was not smaller than 15 mm otherwise the energy from the power supply would be directed into heating the electrodes and not for creating and maintaining the plasma.

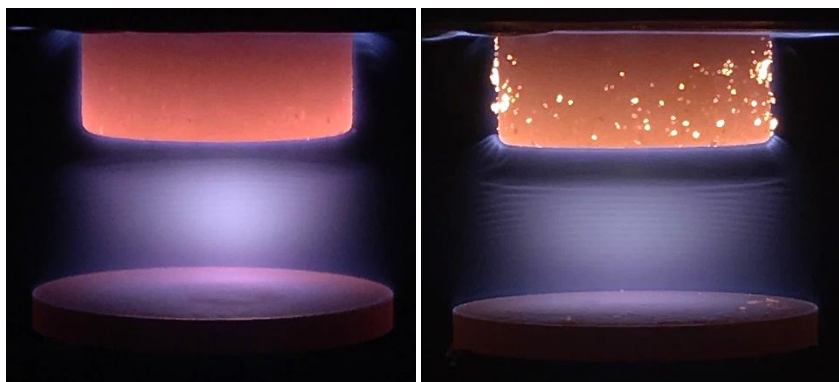


Figure 15. Image of the cathode, substrate and plasma during the 1 hour trial Highest Growth Rate (HGR) run (left), and 3 hour HGR run (right).

Tungsten was used as the material for the substrate and electrodes due to its high thermal stability (melting point = 3420°C ^[126]). Furthermore, the power from the plasma could be well distributed across the substrate due to tungsten's high thermal conductivity. The material has a low coefficient of thermal expansion ($4.2 \times 10^{-6} \text{ K}^{-1}$),^[127] which helped to minimise the thermal mismatch of the metal substrate to the diamond grown, reducing the chance of delamination of the diamond films upon cooling.

During growth runs, arcing of the plasma from the cathode to the substrate was an issue. One reason for the arcing could have been due to the sharp edges of cathode, which concentrate the field lines of the electric charge from the power supply and offer a preferred route for the plasma. To hinder this effect, the edges of the cathode were chamfered after the Taguchi runs were completed (**Figure 16**). To test if the chamfering had helped, a repeat of one of the unsuccessful runs from the Taguchi optimisation was conducted. Run 13 had ended prematurely (2 minutes into the growth) due to consistent arcing from the cathode to the substrate, causing instability in the plasma. The run had lasted 2 minutes before arcing out, whereas after chamfering the cathode edges, the run lasted 8 minutes. These results could indicate a slight increase in the stability of the plasma but are deemed inconclusive, as it is difficult to confirm from these results alone whether the cause of the extended growth time was due to the cathode chamfering, or if the conditions for the run were inherently going to form an unstable plasma that terminates between 2-8 minutes. Due to time constraints, further repeats could not be made, however this would be necessary to establish a more meaningful result.

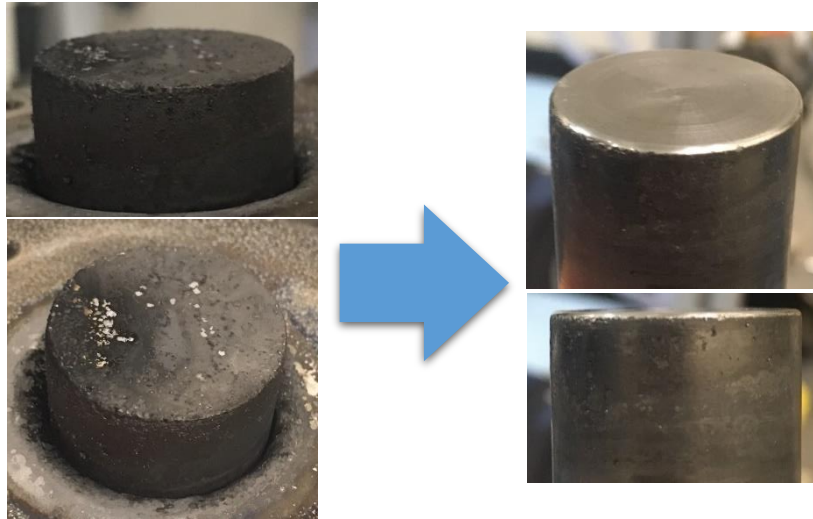


Figure 16. Before and after chamfering the cathode edges.

3.2 Optimisation and characterisation of the diamond thin films

3.2.1 Analysing the Taguchi runs

After each Taguchi run, the substrates were analysed by Raman spectroscopy and SEM. The variation in the quality of the diamond growth across the substrate was assessed by analysing the presence and relative intensities of peaks arising from diamond and different deposited carbon impurities from the Raman spectra. The fewer the number of peaks arising from carbon impurities and the smaller their intensity compared to the diamond peak, the better quality the diamond growth.^[128]

Figure 17 shows an image of the substrate from run 4, and the 13 colour-coded positions on the substrate in which Raman spectra were recorded.

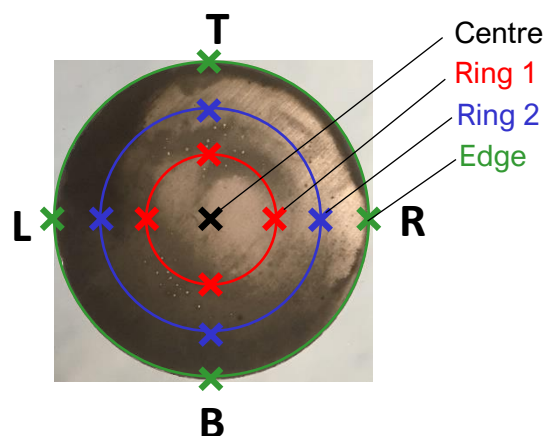


Figure 17. Positions (marked by crosses) on the substrate from run 4 in which Raman spectra were recorded.

The Raman spectrum (**Figure 18**) recorded at the centre point of the substrate shows a sharp peak at 1332 cm^{-1} characteristic to diamond,^[129] a broad peak arising from trans-polyacetylene^[130] between $1430\text{-}1470\text{ cm}^{-1}$ and a broad peak arising from amorphous carbon between $1500\text{-}1600\text{ cm}^{-1}$, known as the G-band.^[129] The trans-polyacetylene domains, formed between grain boundaries, and the G-band both arise from stretching modes between sp^2 hybridised carbon bonds in the structures, which are shifted higher in vibrational frequency than that of diamond due to the stronger bonding between sp^2 carbons than sp^3 carbons. The diamond growth at this point on the substrate can be considered high quality due to the low intensity of the peaks arising from carbon impurities relative to the strong diamond peak.

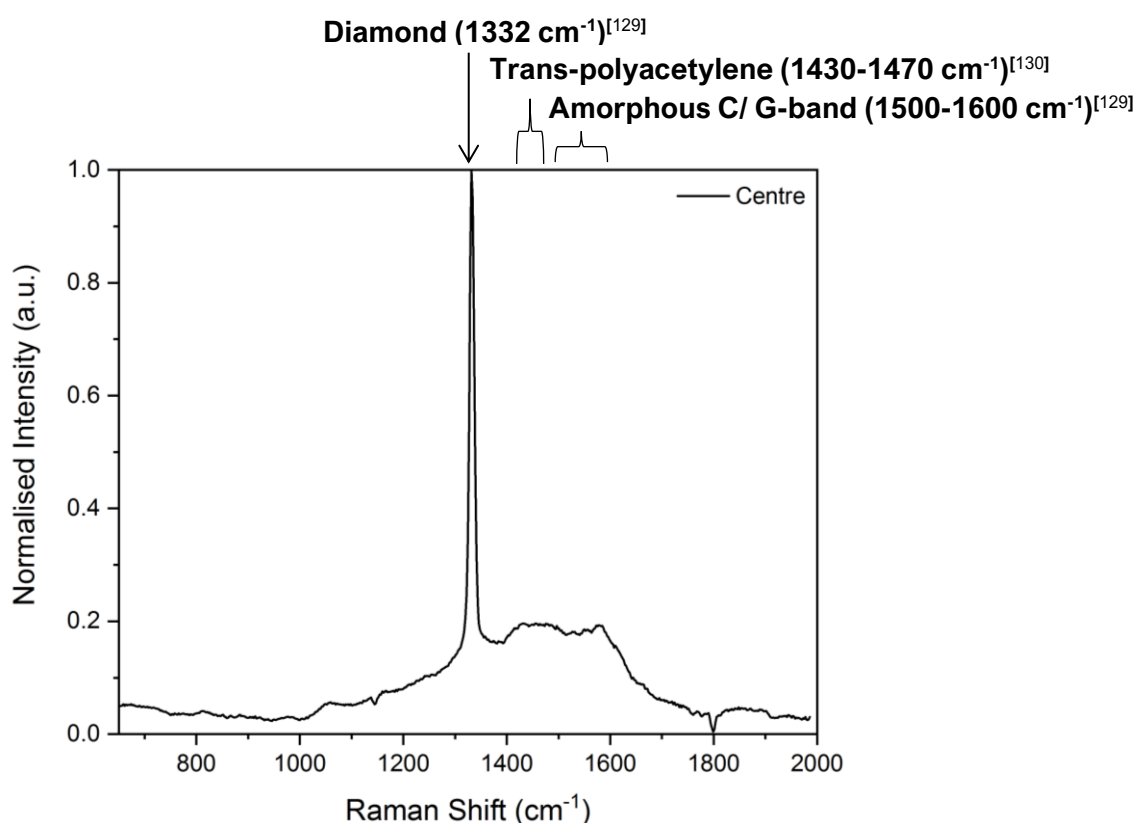


Figure 18. Raman spectrum of the centre position on the diamond substrate from run 4.

The variation in carbon impurities and growth coverage across the substrate can be visualised by **Figure 19**, which shows all 13 Raman spectra of the substrate from run 4. The peaks corresponding to tungsten^[131] and tungsten oxide^[132] at 950 cm^{-1} and 800 cm^{-1} , respectively, appear where the substrate was exposed due to sparse growth⁵. A small amorphous carbon peak at 1345 cm^{-1} , also known as the D-band,^[129] arises from disorder in the graphitic structure. This is caused by impurities such as nitrogen atoms, sp^3 hybridised carbons and dangling sp^2 hybridised carbon bonds, which induce structural imperfections and defects.^[133] The D-band can also be attributed to the ring ‘breathing’ modes of carbon rings in the graphite sheets.^[134]

⁵ The Raman spectrum of a clean tungsten substrate for reference is shown by **Figure 36** in the appendix.

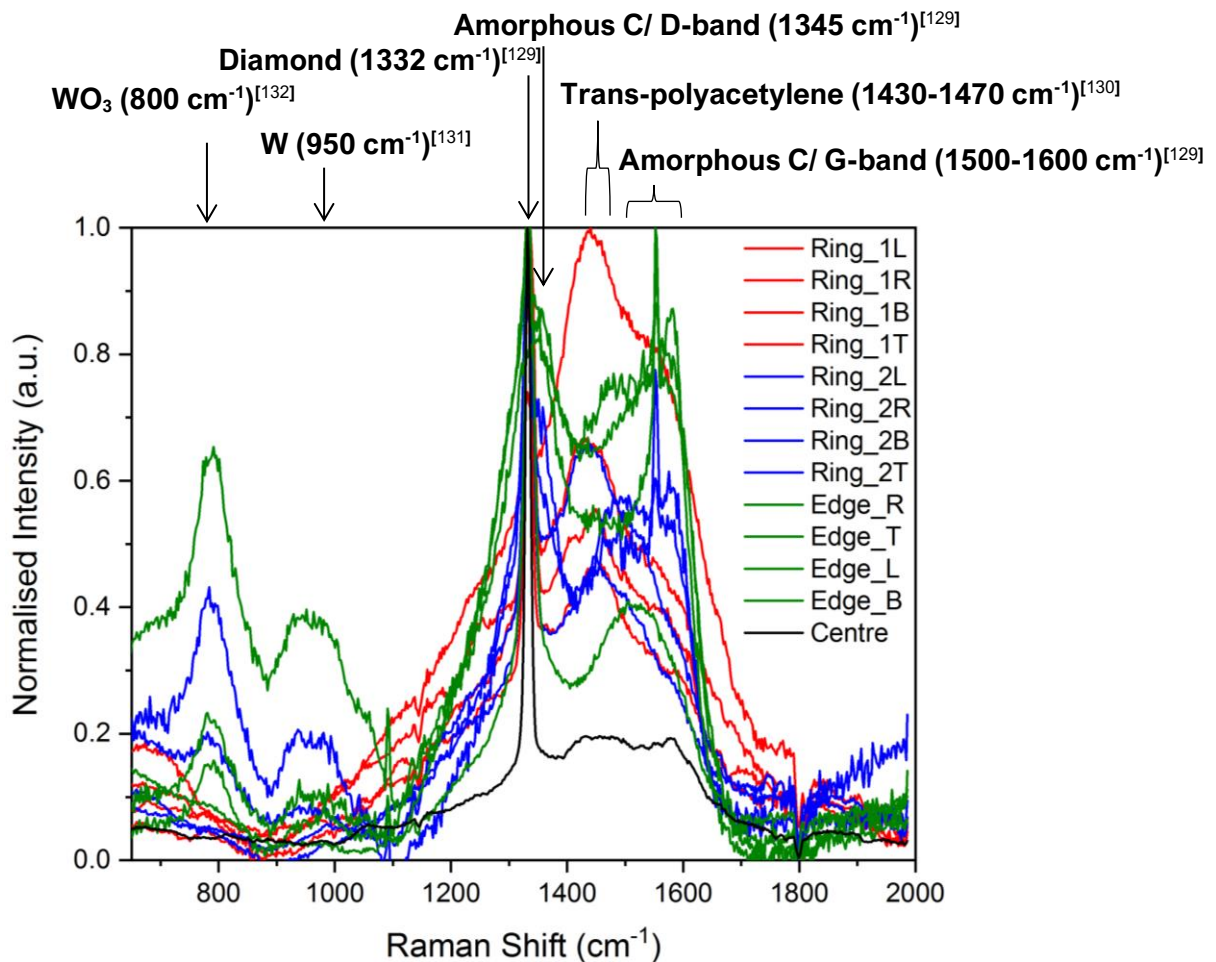


Figure 19. Raman spectra shows growth variation across the substrate from run 4.

The general trend from the Raman spectra across the 16 Taguchi runs showed that the diamond quality was best at the centre of the substrate and decreased moving toward the edge. This may be because the diameter of the electrodes was smaller than the substrate by 0.85 cm, which meant that the plasma may not have fully covered the substrate, leading to a variation in power (and hence temperature) across the substrate. Furthermore, as the ground electrode was not in contact with the entire substrate, the water-cooling by the copper jacket could have been less efficient at cooling the edges of the substrate than the centre. However, as the exact temperature of the substrate or plasma was not recorded, and the only estimate of the temperature was by glow of the substrate, it is not possible to define how the conditions changed exactly across the substrate.

In addition, arcing to the edges of the substrate from the cathode was an issue throughout the Taguchi optimisation, so this could have had a detrimental effect on the growth. As the cathode steel water-cooling jacket was not as efficient at cooling as the copper jacket surrounding the ground electrode, the cathode would glow hot at the relatively high powers used for growth (3.7 - 4.15 kW). As seen in the literature,^[114] high temperatures ($\geq 1100^\circ\text{C}$) favour graphite formation, which would build up on the cathode over the course of the growth run and fall onto the substrate (see **Figure 15**). As graphite is a good electrical conductor (its electrical conductivity is ≈ 15 orders of magnitude greater than that of

diamond),^[135,136] it would act as an arc-point once fallen onto the substrate. Consequently, this had a damaging effect on the quality of diamond grown during the runs.

The effect of power on the diamond quality can be assessed in terms of the effect of substrate temperature on the crystal morphology. Well-defined faceted diamond can be considered better quality than ballas diamond, as graphitic carbon tends to form with ballas diamond. This is shown by the presence of amorphous carbon peaks in Raman spectra, which indicates poor quality diamond.^[118] Despite the shortage of work reported on substrate temperature and crystal morphology using PDC PE-CVD, the general trend in diamond morphology can be seen across multiple plasma CVD systems in which an increase in substrate temperature leads to a change in crystal shapes from triangular (111) facets to cubic (100) facets. Boudina *et al.* reported diamond growth using DC plasma jet CVD, and found triangular facets were formed at substrate temperatures between 650-800°C, and that square and rectangular facets were observed at substrate temperatures between 850-1050°C.^[119] A report of diamond growth using DC arc discharge CVD showed that an amorphous carbon peak was observed by Raman spectroscopy between substrate temperature 600-750°C, which disappeared as temperature increased above this.^[56] This was supported by Suzuki *et al.*, whose work with DC plasma CVD showed amorphous diamond forms below 600°C.^[120] Furthermore, 850°C was found to be the optimal substrate temperature for growth rate and diamond quality using MW PE-CVD,^[121] which is in accordance with the previously mentioned literature. The optimum temperature for growth can thus be estimated to be between 750-1050°C.

SEM images of the substrates from the Taguchi runs provided information on the coverage, growth rate and diamond quality. Like the Raman spectra, the images showed the variation in carbon deposits across the substrates by the range of morphology from cubic-faceted diamond and ballas diamond, to graphitic amorphous carbon. **Figure 20** shows how the diamond morphology changes with substrate temperature, methane concentration and pressure.^[137]

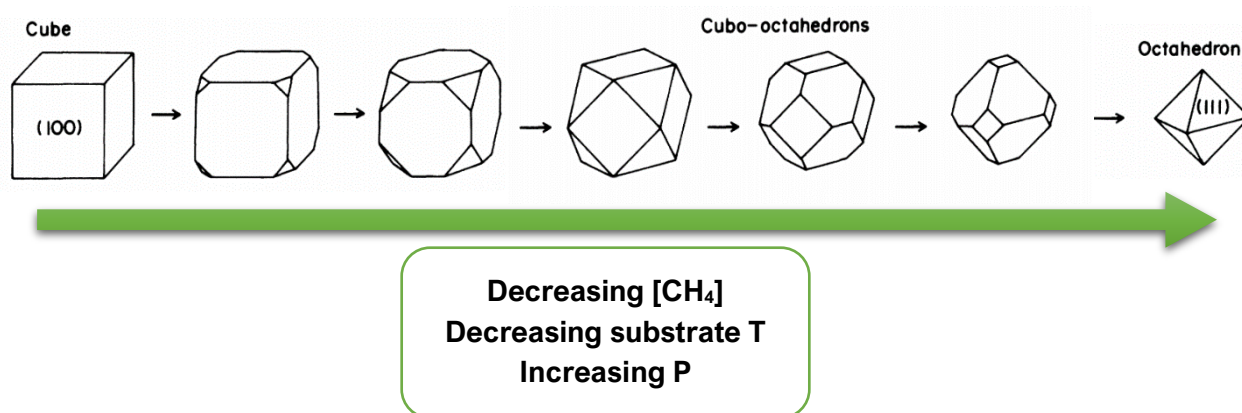


Figure 20. Schematic diagram showing the variation in diamond morphology depending on methane concentration, substrate temperature and pressure. Edited diagram by Kobashi *et al.*^[137]

It has been reported that pulse frequency does not have a significant effect on the diamond morphology.^[138,139] The influence of argon concentration on the morphology and size of the crystals is fairly inconclusive, as several papers show contradicting results. Shih *et al.* reported that the size of crystals tends to increase and the morphology changes from octahedral to cubic with an increase in argon concentration from 20-60% in an H₂/Ar/CH₄ mix grown by MW PE-CVD.^[123] Conversely, polycrystalline films grown by MW PE-CVD using 40% argon have shown no significant change in the morphology from the films grown using the same conditions but with no argon present.^[40] In both reports, the morphology was observed across larger differences and much higher argon concentrations (0-60%) than those used in this experiment (0-3.7%), which could suggest that at such low argon concentrations, the effects of argon on the changes in morphology or crystal size between runs may not be visible.

The generally accepted trend is that as the pressure increases, and the substrate temperature and methane concentration decrease, the CVD diamond morphology changes from cubic (100) faceted to octahedral (111) faceted diamond.^[38,119] In between, cubo-octahedral faceted diamond occurs by different ratios of the (100) facet and (111) facet. This trend can be observed by comparison of the SEM images of the substrates from run 3 and run 4 (**Figure 21**).

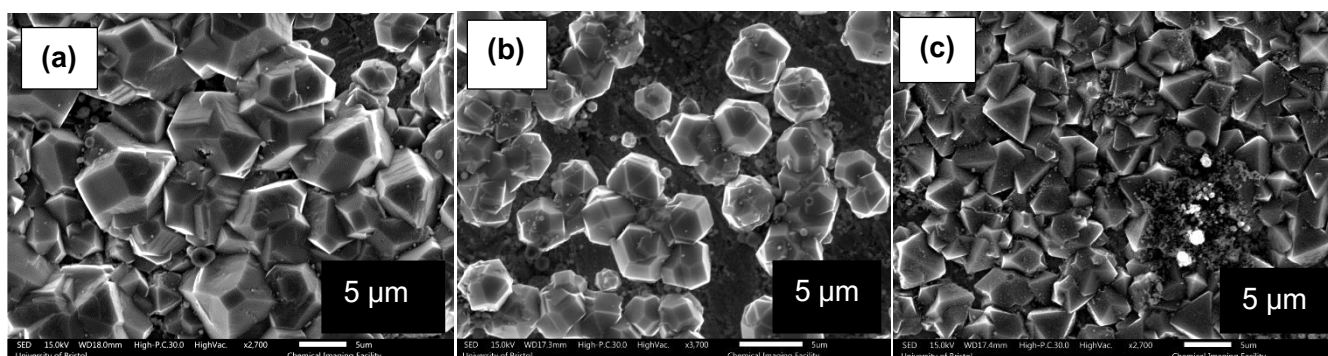


Figure 21. SEM images of substrate from run 4 ((a) and (b)) and from run 3 ((c)).

The pressure was 130 Torr for both runs, and the power, methane concentration, argon concentration and pulse frequency were 4.15 kW, 3.7%, 3.7% and 125 kHz for run 4, and 4 kW, 2.9%, 1.9% and 150 kHz for run 3. The diamond morphology from run 4 is cubo-octahedral, a mix of triangular and square facets, whereas the diamond morphology from run 3 is predominantly octahedral with triangular facets. As power (and hence substrate temperature) and methane concentration are both lower for run 3 than run 4, this supports the trend for a change in morphology toward octahedral facets. As the effect of pulse frequency on diamond quality is fairly insignificant, the change of 25 kHz between runs can be assumed to have negligible effect on the morphology.

Figure 22 shows several SEM images demonstrating the variation in diamond growth across runs. Images (a), (b) and (e) show so-called ‘cauliflower-like’ or ballas diamond, which can form when methane concentration is too high or if pressure or atomic hydrogen concentration is low.^[123,118] Image (c) shows that a layer of microcrystalline diamond has formed, perhaps acting as nucleation sites for the larger cubo-octahedral crystals that have grown on top. Image (d) shows the point at which an arc has hit, and cleaned diamond off the substrate.

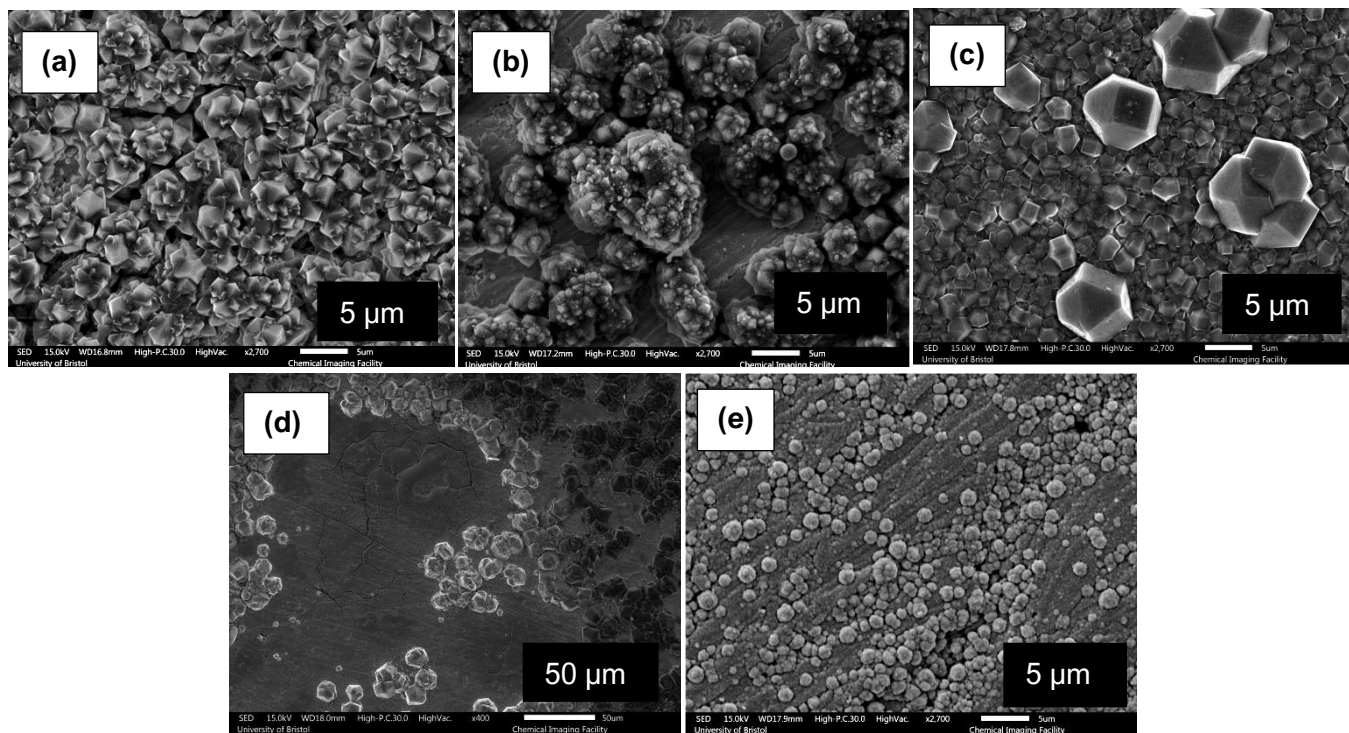


Figure 22. SEM images from various Taguchi runs. (a) and (b): run 5, (c): run 8, (d): run 9 and (e): run 10.

A general trend in the optimisation showed that as the pressure was increased above 130 Torr, the plasma stability decreased and arcing to the substrate from the cathode increased. This meant that only 5 out of 16 runs lasted the full 1 hour growth duration⁶, which did have a detrimental effect on the accuracy and effectiveness of the optimisation.

⁶ See appendix **Table 10** for details of the conditions, duration time and growth rates for each Taguchi run.

3.2.2 Optimisation for Highest Quality Diamond (HQD) growth conditions

The optimum conditions for HQD growth were calculated by estimating the full line-width at half maximum (FWHM) of the diamond peak (1332 cm^{-1}), from the Raman spectra of the Taguchi runs. Broadening of the diamond peak is indicative of scattered light from defects, so the sharper the diamond peak (and hence the smaller the FWHM), the nearer the diamond is toward a perfect crystalline structure void of defects. The FWHM for a pure diamond crystal, which was used for calibration of the Raman instrument⁷, was estimated to be 9.5 cm^{-1} . This serves as a reference for comparison with the FWHM of the diamond grown in the Taguchi runs and the optimised growth runs. If a diamond peak was present in the Raman spectra, the ratio of the intensity of the amorphous carbon (G-band) peak ($1500\text{-}1600\text{ cm}^{-1}$) to the intensity of the diamond peak was also calculated. The ideal conditions would have the lowest value for both FWHM and the ratio of intensities. Raman spectra that had a diamond peak FWHM $\leq 40\text{ cm}^{-1}$ were considered acceptable to include in the optimisation plots, due to the large uncertainty in the estimation, which permitted including only 4 runs out of the 16. This meant that the plots contained between 2-4 data points, and hence did not present highly accurate relationships between the control parameters and the quality of the diamond. Nevertheless, the optimised conditions for HQD, which were determined by the optimisation plots (**Figure 23**), are displayed in **Table 6**.

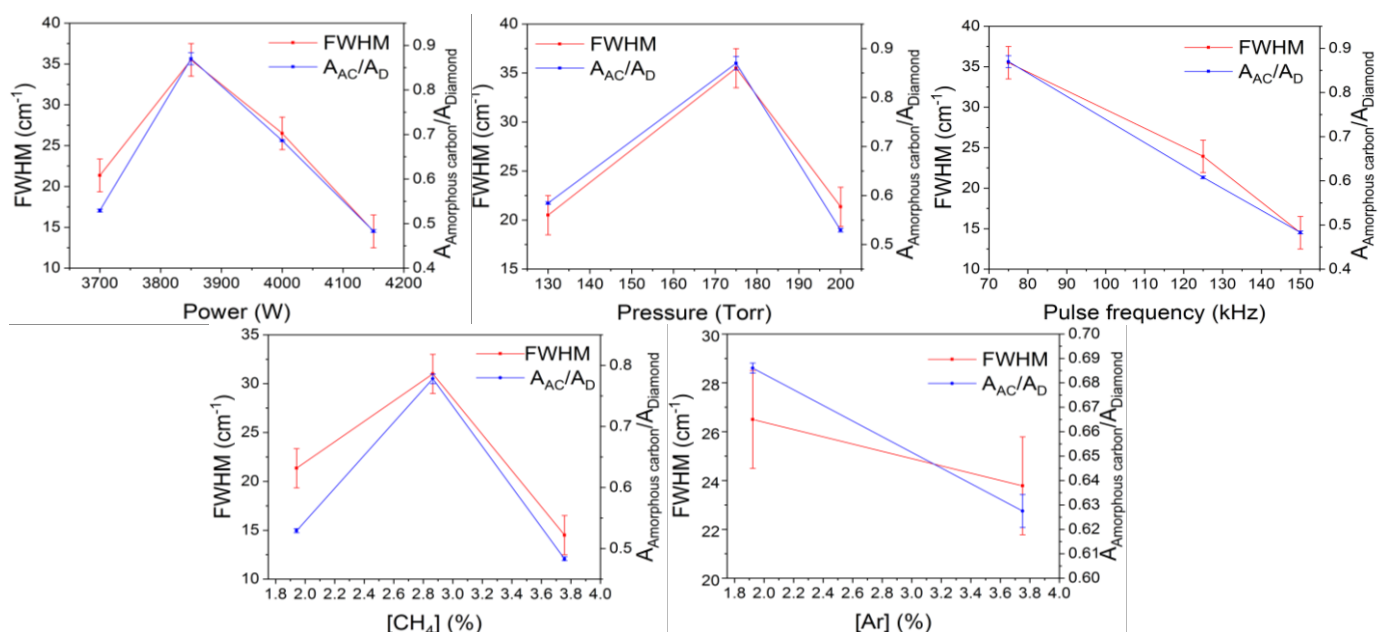


Figure 23. Plots showing the relationship between quality of diamond growth and each control parameter.

Table 6. Optimised conditions for HQD.

Pressure (Torr)	Power (kW)	Pulse Frequency (kHz)	[Ar] (%)	[CH ₄] (%)	Voltage (V)	Current (A)	Duration (min)
130	4.15	150	3.7	3.7	430	9.7	180

⁷ See appendix **Figure 35** for the Raman spectrum of the diamond crystal used for calibration.

Due to the insufficient number of data points and large error associated with some data points, the optimum pressure was unclear from the plot. As both the FWHM and ratio of intensities were valid indicators of diamond quality, and the lowest values for both were 130 Torr and 200 Torr respectively, both pressures were tested. Initially, the pressure for optimised growth was set to 200 Torr for the 1 hour trial growth run, however the plasma was unstable and terminated after 12 minutes. When the run was repeated with pressure set to 130 Torr, the plasma was much more stable and the run lasted the entire 1 hour.

During the 3 hour growth run using the optimised conditions, the plasma appeared relatively stable, covering the majority of the substrate. The substrate was glowing red, which did not occur to such an extent during any of the Taguchi runs, and the voltage was steady at 430 V. The glowing substrate could be the product of a more stable plasma which allowed a more efficient transfer of energy into the substrate. This could have been achieved by the good combination of conditions used and the reduction of arcing by chamfering the cathode before the run. Some arcing occurred from the cathode to the edges of the substrate, but this appeared to be due to graphite falling from the cathode onto the substrate and subsequent arcing to the graphite flakes, and not from instability in the plasma.

The substrate was analysed by Raman spectroscopy and imaged by SEM. **Figure 24** shows the Raman spectrum of the highest quality diamond grown on the substrate at position Ring_1B, which has an estimated FWHM of 15 cm^{-1} , and a ratio of the peak intensity of amorphous carbon to diamond of 0.3. Compared to the FWHM of the reference diamond (9.5 cm^{-1}), the quality of the diamond was not perfect, however it was generally better than the highest quality growth achieved by the Taguchi runs (which had a FWHM of 14.5 cm^{-1} , but a ratio of intensities of 0.5).

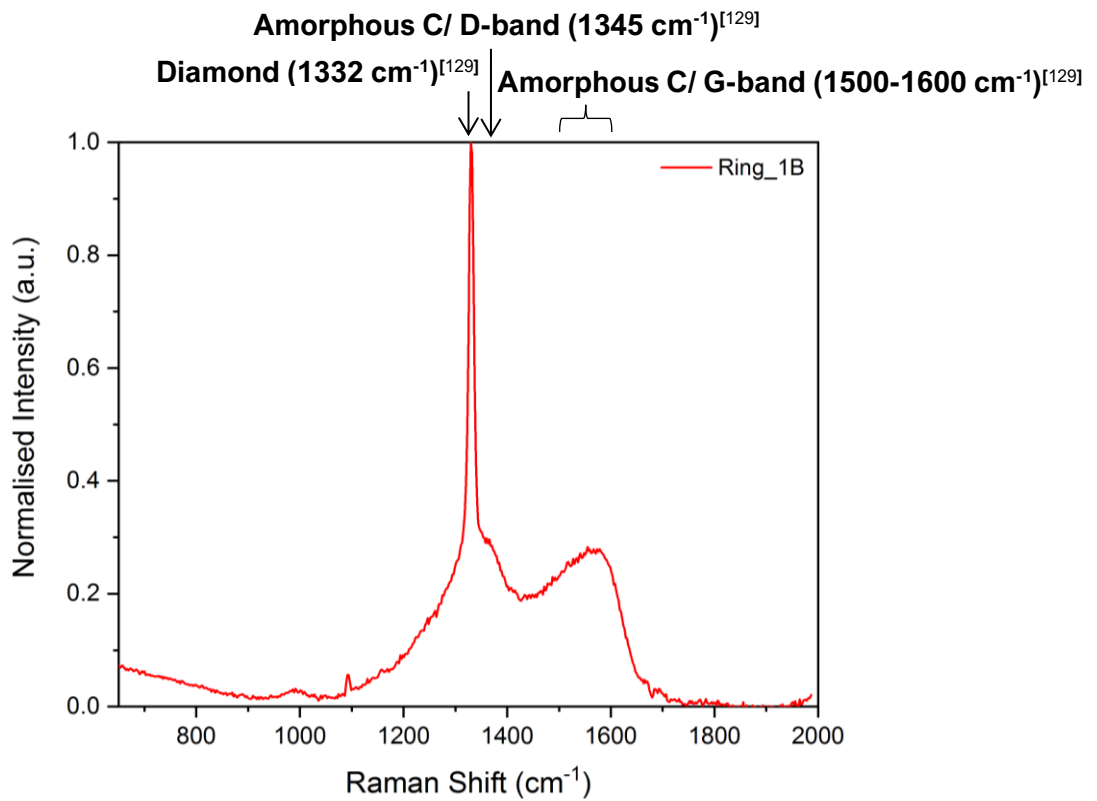


Figure 24. Raman spectrum of position Ring_1B on substrate from the 3 hour HQD run.

Figure 25 shows all the Raman spectra recorded across the substrate.

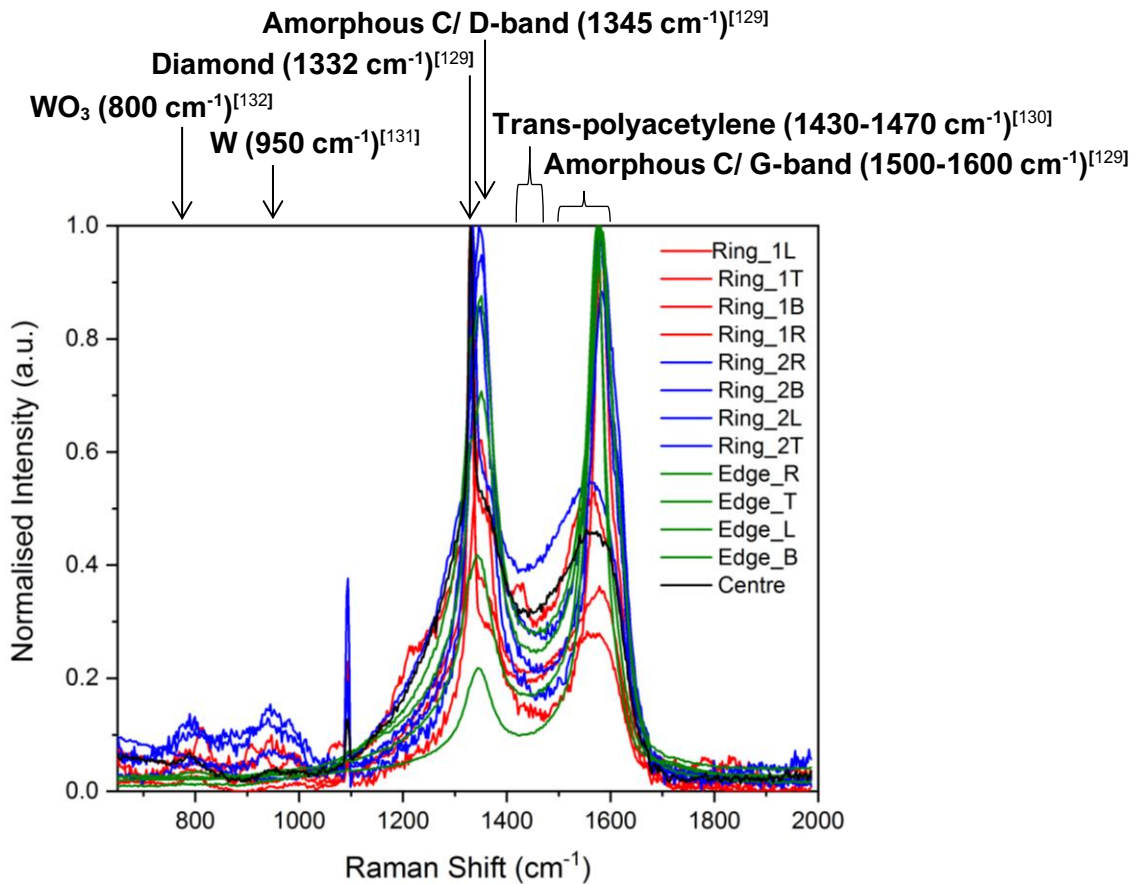


Figure 25. Raman spectra showing the variation in diamond quality across substrate from the 3 hour HQD run.

The average diamond peak FWHM is 22.5 cm^{-1} and the average ratio of peak intensities is 0.4. By comparison with an average FWHM and ratio of intensities of all of the Taguchi runs, which was 24.5 cm^{-1} and 0.6 respectively, the average quality of diamond grown by the HQD conditions was better. However, the amorphous carbon peaks (G- and D-bands) were fairly dominant across the substrate, which most likely indicates that the methane concentration was too high. As confirmed by the SEM images (**Figure 26**), the growth was mainly ballas diamond (image (a)), which is formed in conditions close to those of amorphous carbon.^[140]

From analysis of the plots, it appears that the higher the argon concentration, the better the quality of diamond grown. However, as the relationship is based upon two data points, this is not a very reliable result, and further tests would have to be conducted to gain a stronger relationship. As was reported on in the literature,^[138,139] pulse frequency does not tend to have a big effect on the quality of diamond growth, however it has been reported that the substrate temperature increases with an increase in the pulse frequency. The results from the optimisation show that diamond quality increases with increasing pulse frequency, so this may be the result of an increase in substrate temperature to an ideal temperature for high quality diamond growth. However, without using a pyrometer to take accurate temperature measurements, a conclusion cannot be drawn from these speculations alone.

Due to the instability of the plasma at higher pressure, the growth could not be carried out at 200 Torr, which according to the optimisation plots, could have shown higher quality diamond growth than the lower pressure used. As the generally accepted trend is that ballas diamond is formed when pressure is too low, which is evident from the SEM images of the HQD run, the higher pressure (at 200 Torr) could have shifted the conditions to favour growth of cubic or octahedral facets. However, due to the lack of data points, the indication of higher quality growth at 200 Torr from the optimisation plot could have been an anomalous result, so more tests and repeats would be necessary to gain a more accurate relationship between pressure and quality of diamond.

The optimisation for power showed that a higher power produces higher quality diamond. This is in agreement with the trend that at higher power (and hence substrate temperature), square faceted diamond is favoured. However, the SEM images (**Figure 26**) show predominantly ballas diamond growth on top of large cubic crystals (image (a)), in addition to small octahedral facets (image (d)). This may be because the combination of low pressure, high power and high methane concentration pushed the morphology of ideal growth past cubic-faceted and towards ballas diamond. It has been shown by MW PE-CVD that an increase in substrate temperature between $800\text{-}950^\circ\text{C}$ can have the effect of amplifying the effect of methane saturation on the system, increasing the likelihood of ballas diamond formation.^[141] The red-glowing substrate observed during the 3 hour run could indicate that the temperature of the substrate was high enough to have this effect. The small octahedral crystals (image (d)) were imaged nearer the edge of the substrate, where the plasma may not have been concentrated

on the substrate. Hence, the substrate temperature and methane concentration could have been lower there, which would push toward octahedral-faceted growth.

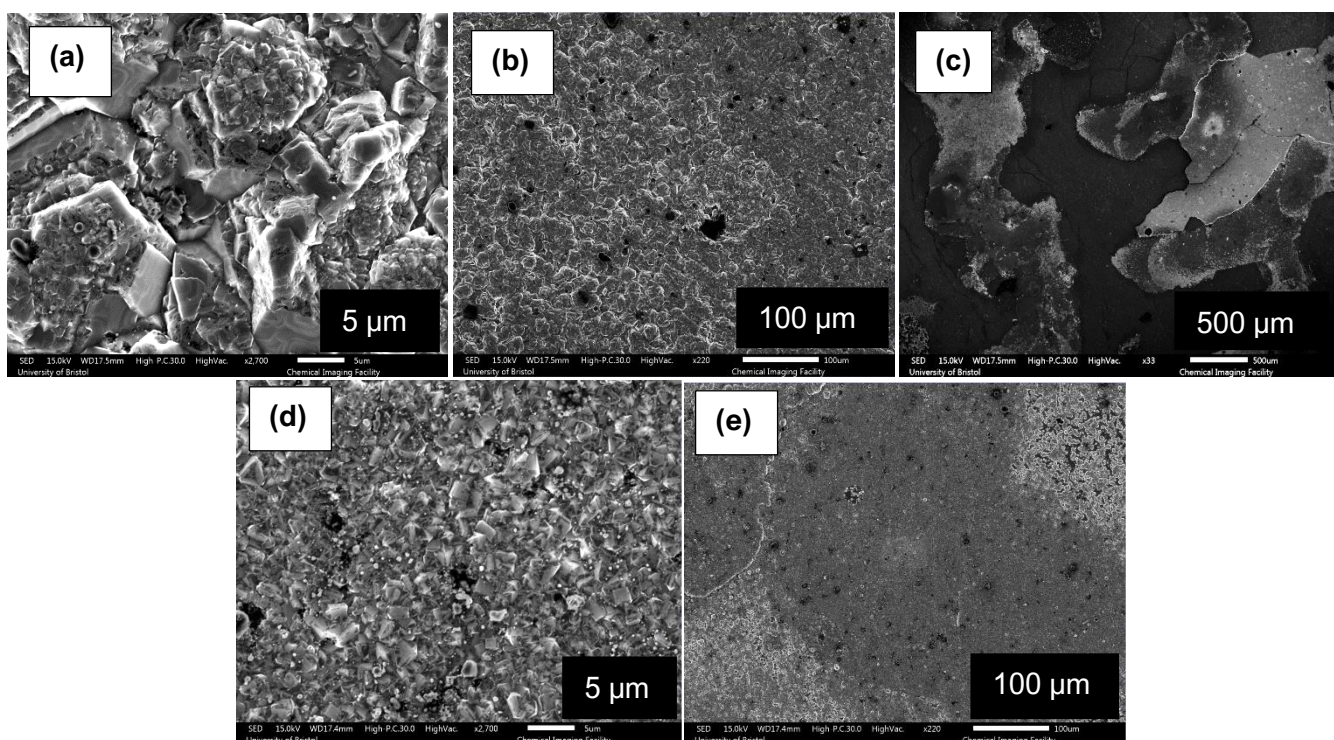


Figure 26. SEM images from the 3 hour HQD run. (a) is a magnified area of (b), and similarly (d) is a magnified area of (e).

It can be theorised from the optimised conditions that a 3.7% methane concentration would produce the best quality diamond. Across the literature, the trend shows that if the methane concentration becomes too high, ballas diamond and graphite will form.^[118,142] As the diamond growth is dependent on the combination of conditions, and not necessary each condition separately, a methane concentration of 3.7% was most likely too high for this combination of conditions, giving ballas diamond, but would have been the ideal concentration to produce better quality diamond if combined with a different set of conditions, which is a limiting feature of the Taguchi optimisation.

The evidence that a thin film was formed can be seen by the weak intensity of the peaks arising from tungsten and tungsten oxide from the Raman spectra, which indicated good coverage across the substrate. This can be confirmed by the SEM images, which show even coverage, in addition to delamination of the film (**Figure 26** image (c)) that had occurred due to thermal mismatch of diamond to tungsten upon cooling. The growth rate was estimated to be $6.9 \pm 4.8 \mu\text{m h}^{-1}$, which is slightly higher than the average growth rate from the total Taguchi runs ($4.1 \pm 1.5 \mu\text{m h}^{-1}$).

3.2.3 Optimisation for highest growth rate (HGR) conditions

To measure growth rate for each Taguchi run⁸, the crystal sizes were estimated from the SEM images for each run and divided by the duration of the run. As there weren't enough tungsten substrates to use a new one for each Taguchi run, some of the substrates had to be cleaned and re-used. It was clear from the SEM images that several runs had diamond growth on the substrate that was just residual from old growth runs. This was evident by the diamond appearing very damaged, pitted and covered in soot. Furthermore, several runs, such as one that lasted no more than 8 minutes, showed 'growth' that would correspond to unrealistically high growth rates compared to the rest of the Taguchi runs. This was evidently old growth and so these runs (5, 9 and 14) were discounted from the analysis.

The growth rate was plotted against each control parameter (see **Figure 27**), and the value for each parameter that corresponded to the maximum growth rate was recorded. The optimised conditions for HGR are detailed in **Table 7**.

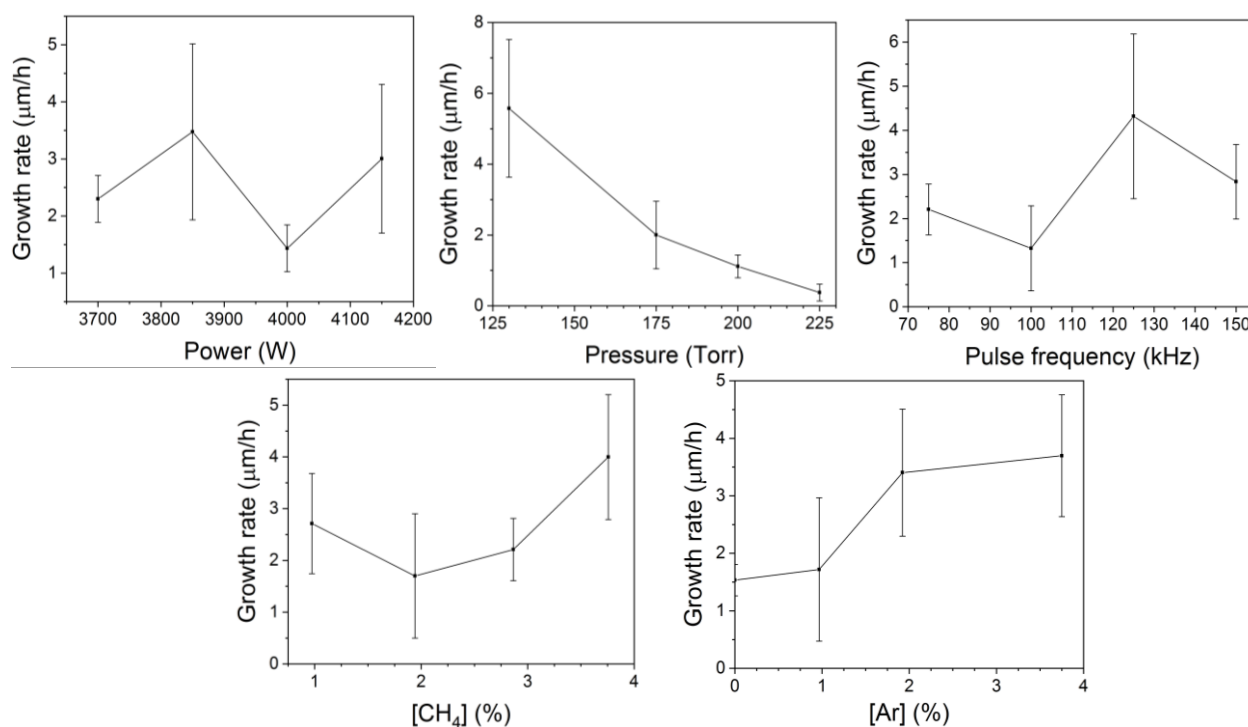


Figure 27. Plots showing the relationship between growth rate and each control parameter.

Table 7. Optimised conditions for HGR.

Pressure (Torr)	Power (kW)	Pulse Frequency (kHz)	[Ar] (%)	[CH ₄] (%)	Voltage (V)	Current (A)	Duration (min)
130	3.85	125	3.7	3.7	430	9.0	180

⁸ See appendix, **Table 10** for details on the growth rate of each Taguchi run.

During the 3 hour growth run, the plasma was stable, covering the majority of the substrate, and the voltage stabilised at 430 V. In a similar way to the Highest Quality Diamond (HQD) optimised run, the substrate glowed a dull red, and graphite falling from the cathode to the substrate, and subsequent arcing from the cathode to the graphite flakes, was the main source of arcing. **Figure 15** shows the cathode and substrate during the 1 hour trial run and 3 hour run, both using conditions optimised for HGR, and the graphite build-up on the cathode which glows brightly. The stability of the plasma was most likely due to a good combination of conditions and the chamfering of the cathode edges prior to the growth run.

Figure 28 shows the Raman spectra of the highest quality diamond grown on the substrate at position edge_T, which had a FWHM of 15 cm^{-1} , with a ratio of peak intensities of 0.2. Compared to the FWHM of the pure diamond reference (9.5 cm^{-1}), the diamond was not the highest quality, however the quality is better than the highest quality diamond growth from the Taguchi runs (which had a FWHM of 14.5 cm^{-1} , but a ratio of intensities of 0.5). Furthermore, the quality of the diamond at this position on the substrate was marginally better than the highest quality diamond grown during the optimised HQD run, despite the fact that the conditions were not specifically optimised for diamond quality. This is most likely because of the large uncertainty associated with the data points in the optimised quality plots and the lack of data, leading to poor representations of the relationships between the quality of diamond and each control parameter.

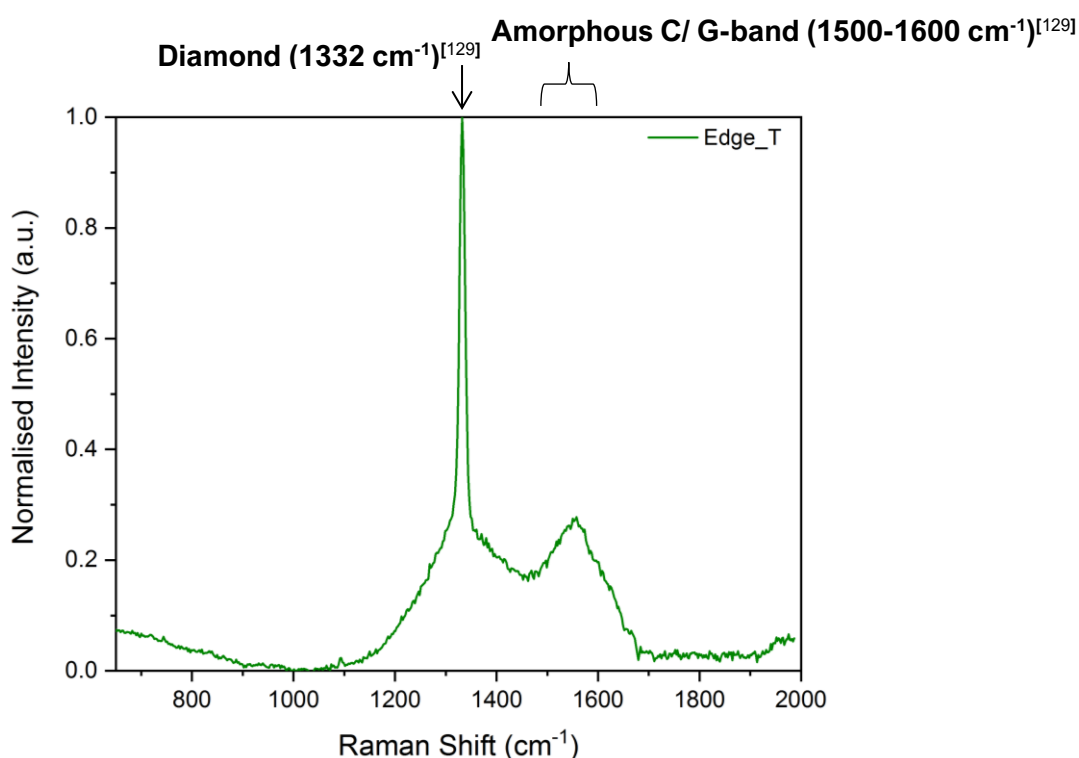


Figure 28. Raman spectrum of Edge_T position on the substrate from the 3 hour HGR run.

Figure 29 displays the Raman spectra recorded across the substrate, showing the variation in diamond growth. The average FWHM across the substrate was 21 cm^{-1} , with a ratio of peak intensities of 0.5. This was better quality than the average of the total Taguchi runs, which had an average FWHM of 24.5 cm^{-1} and a ratio of intensities of 0.6. Generally, the diamond that had grown on the substrate was good quality, however there was a wider range of carbon deposits across the substrate compared to optimised HQD growth. Trans-polyacetylene had a strong presence, which could be due to the larger crystals that had grown (see **Figure 30**), and hence a larger area of grain boundaries for the trans-polyacetylene to grow between. The tungsten and tungsten oxide peak intensities appeared low, indicating a more even, fuller coverage of growth over the substrate.

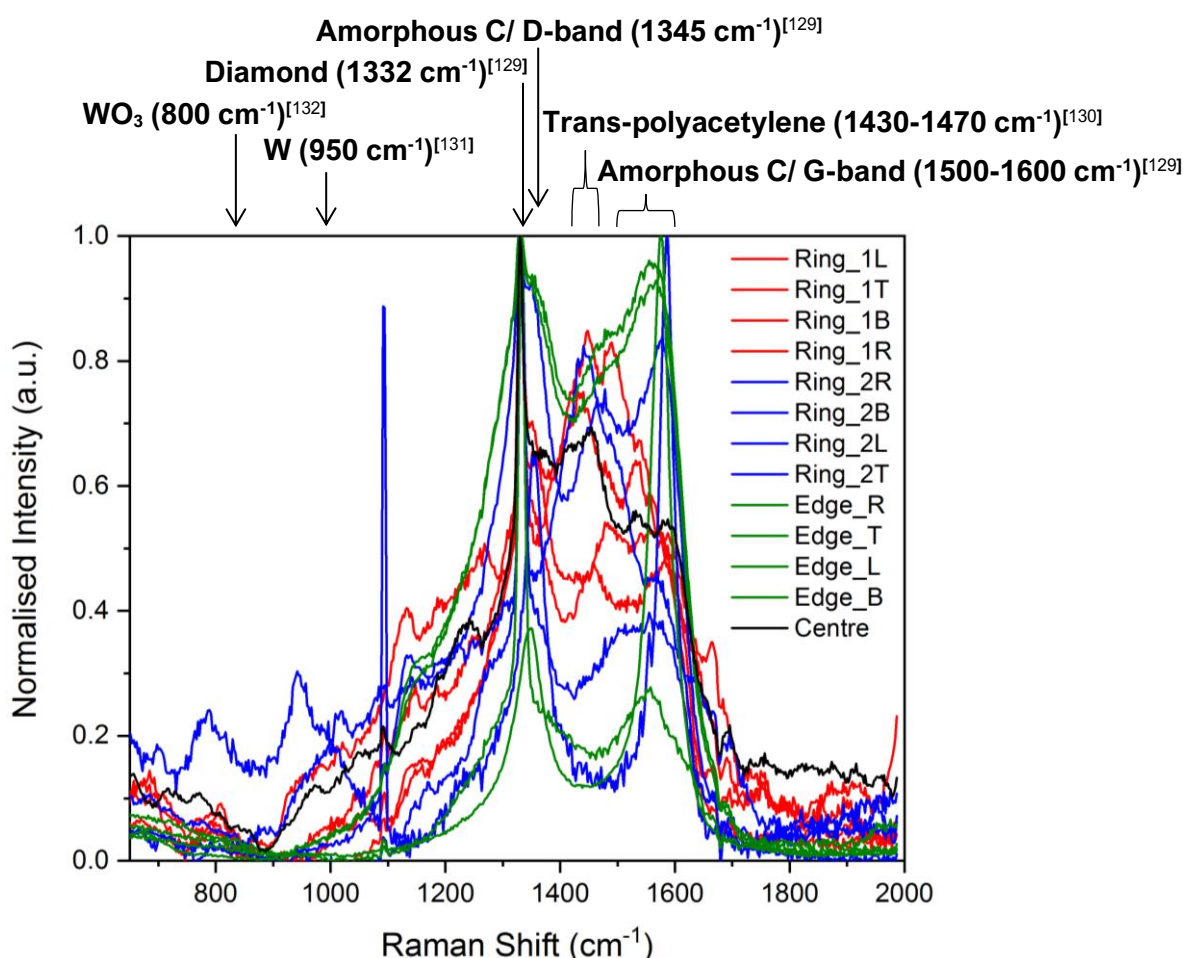


Figure 29. Raman spectra of the substrate from the 3 hour HGR run. The peak at 1100 cm^{-1} is due to background scattered light.

The SEM images (**Figure 30**) showed the formation of large cubic and cubo-octahedral facets, and an even coverage of growth. The growth rate was estimated to be $9.8 \pm 3.7\ \mu\text{m h}^{-1}$, which was larger than the average growth rate from the total Taguchi runs ($4.1 \pm 1.5\ \mu\text{m h}^{-1}$), and the growth rate of the diamond from the HQD run ($6.9 \pm 4.8\ \mu\text{m h}^{-1}$), which is good evidence that the optimisation for growth rate was successful.

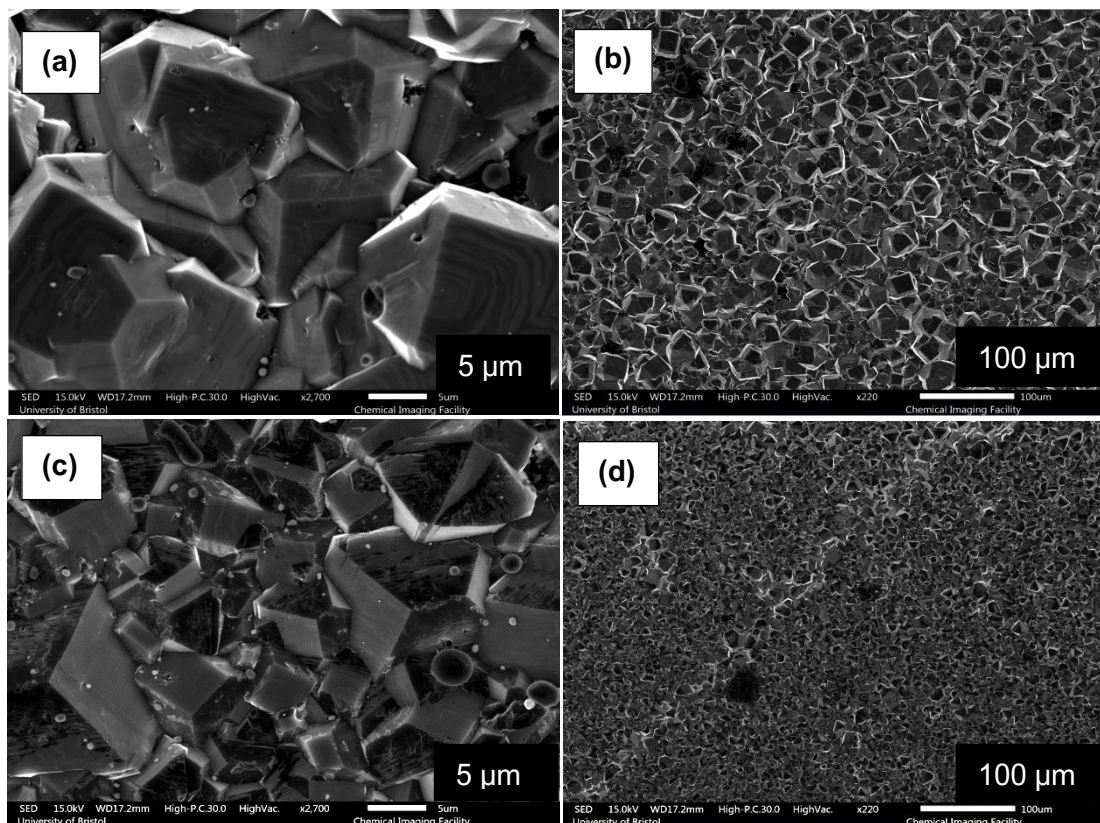


Figure 30. SEM images from the 3 hour HGR run. Image (a) is a magnified area of (b), and (c) is a magnified area of (d).

From the optimisation plots, it can be observed that growth rate increases with increasing methane concentration up to 3.7%. This has been supported by the literature,^[118] which shows an increase in the growth rate with an increase from 0% to 2% methane concentration when the substrate temperature was 950°C, and up to 4% methane when the substrate temperature was 870°C. Surpassing these methane concentrations led to a significant drop in the growth rate, but without further tests using methane concentrations $\geq 3.7\%$, this trend cannot be confirmed by the optimisation. It appears that as the argon concentration increased from 0-3.7%, the growth rate also increased, which supports the results from the literature.^[39-41,44]

As the pressure increased from 130-225 Torr, the growth rate appears to decrease steadily. This is not supported by the literature, which reports that as pressure increases, growth rate also increases, as the reactive carbon species in the plasma become denser with increasing pressure, and more likely to react faster with the growing diamond surface.^[142] The reason for the apparent decrease in growth rate with an increase in pressure is most likely due to the instability of the plasma, and subsequent arcing, as pressure increased above 130 Torr, which hindered the growth of the diamond.

A linear relationship between pulse frequency and diamond growth rate is not observed from the optimisation plot, as the growth rate tends to fluctuate as the pulse frequency increased from 75-150 kHz. There is a slight average increase in growth rate as pulse frequency increased, but more data would need to be collected within the frequency range to determine a more accurate relationship. Similarly, the relationship between power and diamond growth rate is also not clear from the

optimisation plot due to large error in the data. In theory, dissociation of methane molecules into methane radicals with sufficient energy to form diamond is dependent on the power, which means the growth rate should increase with an increase in power. However, as the cathode was becoming too hot at higher power, the plasma was unstable and subsequently the growth was not as optimal as it could have been.

3.2.4 Analysis of the optimised HQD and HGR growth runs by OES

OES was used to detect the species present in the plasma during the 3 hour runs optimised for HQD and HGR. The spectra are shown in **Figure 31** and details of the transitions are shown by **Table 8**. The intensities of the peaks were largely dependent on the position and angle of the spectrometer with respect to the plasma. The position must have been slightly different for both runs, as many of the features seen in spectrum (a) cannot be seen in spectrum (b) due to the difference in intensity of the emission. However, this does not necessarily mean that the same species were not present in the plasma during both runs.

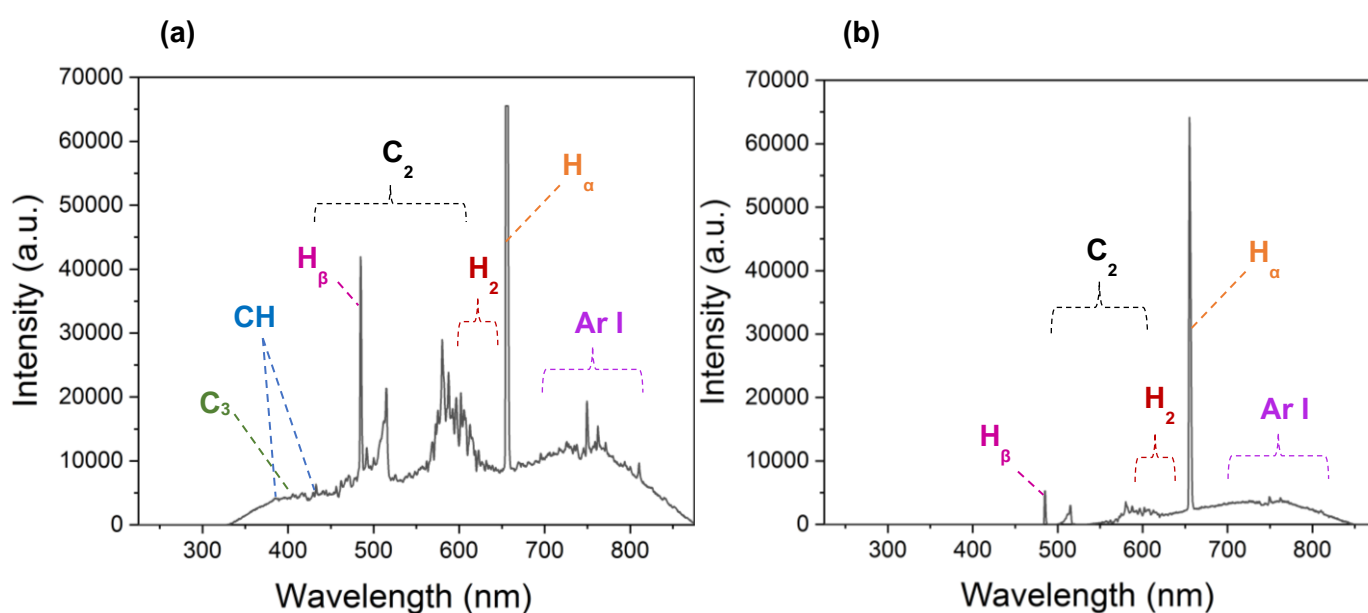


Figure 31. OES spectra of the plasma during the 3 hour runs for (a) HGR and (b) HQD.

In accordance with the literature,^[143] the peaks at 433 nm, 471 nm, 515 nm, 580 nm and 615 nm correspond to the swan bands for the C_2 radical. The small peak at 406 nm arose from the C_3 radical, which has been associated with graphite decomposition.^[144] Small peaks at 386 nm and 433 nm correspond to the CH radicals from methane decomposition.^[145] H_2 can be observed by the Fulcher- α band between 590-640 nm,^[146] but the primary indication for H_2 in the system is by the presence of H_α and H_β transitions from the Balmer series,^[147] which produced high intensity peaks at 655 nm and 485 nm, respectively. The presence of argon in the plasma is evident from the features observed between ≈ 700 -850 nm, which arise from neutral argon atom (Ar I) $4p - 4s$ transitions.^[148,149]

Table 8. Species present in the plasma for the 3 hour optimised runs, and associated transitions and peak wavelengths.

Species	Transition	System	Wavelength (nm)
C ₂	$d^3\Pi_g \rightarrow a^3\Pi_u$ ($\Delta v = +2, +1, 0, -1, -2$)	Swan	441, 471, 515, 580, 615
C ₃	$A^1\Pi_u \rightarrow X^1\Sigma_g^+$	Swings	406
CH	$B^2\Sigma^- \rightarrow X^2\Pi$	Swan	386
CH	$A^2\Delta \rightarrow X^2\Pi$	Swan	433
H _{α}	$n = 3 \rightarrow n = 2$	Balmer	655
H _{β}	$n = 4 \rightarrow n = 2$	Balmer	485
H ₂	$d^3\Pi_u \rightarrow a^3\Sigma_g$	Fulcher- α	590-640
Ar I	$4p \rightarrow 4s$	-	701, 728, 737, 749, 762, 771, 810

Chapter 4: Conclusion and Future Work

A Taguchi optimisation was performed on the modified PDC PE-CVD reactor, after the successful installation of a new copper water-cooling jacket to the ground electrode. The power, pulse frequency, pressure, methane concentration and argon concentration were optimised for highest quality diamond and highest growth rate. Throughout the 16 Taguchi runs, instability of the plasma was the main issue affecting diamond growth, which occurred due to a combination of effects: the cathode becoming too hot, graphite deposits falling onto the substrate and subsequent arcing to the substrate, and if the combination of growth conditions set by the Taguchi optimisation lead to an inherently unstable growth environment.

The results of the analysis of the optimised Highest Quality Diamond (HQD) 3 hour growth run show that the quality of diamond that had grown was better (small FWHM and intensity ratio of amorphous carbon to diamond) than the quality of growth by the Taguchi runs on average, indicating that the optimisation was successful. Furthermore, a thin layer had formed, which is a promising stepping-stone towards growing ¹³C diamond thin films. However, the majority of growth was in the form of amorphous carbon, which is most likely due to the methane and argon concentrations being too high or the substrate temperature too low. The optimisation could have been more accurate if more data from the Taguchi runs could have been considered in the optimisation plots, however due to the combination of conditions or instability in the plasma leading to arcing, not all of the runs grew diamond. The optimal conditions for HQD were as follows: 130 Torr, 4.15 kW, 150 kHz, 3.7% methane, and 3.7% argon.

The results of the analysis of the optimised Highest Growth Rate (HGR) 3 hour run showed that the growth rate had been improved upon, achieving a rate of $9.8 \pm 3.7 \mu\text{m h}^{-1}$. However, due to the adverse effect of plasma arcing on diamond growth, the rate was not as high as it could have been. A thin film of diamond was grown, as observed by the SEM images, however as the plasma did not fully cover the

substrate during both optimised runs, growth was not consistent across the substrate. Unfortunately, due to the time constraints of the project, closed cycle growth conditions were not tested.

In order to achieve more stable growth conditions, and reduce arcing significantly, better water-cooling of the cathode is a necessity. The next step in the project would be the installation of a new water-cooling jacket and subsequent optimisation of the reactor, in which closed cycle growth conditions could be tested in a more stable growth system. Furthermore, the use of a pyrometer to accurately measure the temperature of the substrate during the optimisation would be advantageous, as it would allow for the effect of temperature on diamond quality and growth rate to be quantified. The plasma temperature could be studied by a novel method of OES coupling with Thomson scattering, which has been used as a means of determining electron temperatures and densities in low-pressure argon discharges.^[150] Higher argon concentrations ($\geq 20\%$) could also be experimented with, in order to better place the results in the context of existing literature.^[40,44,123]

Finally, once the reactor has been optimised for isotopically pure ^{13}C diamond growth, it would be important to measure the thermal conductivity and Young's modulus of the diamond, so that the effect of isotope purity on these properties can begin to be constrained.

Appendix

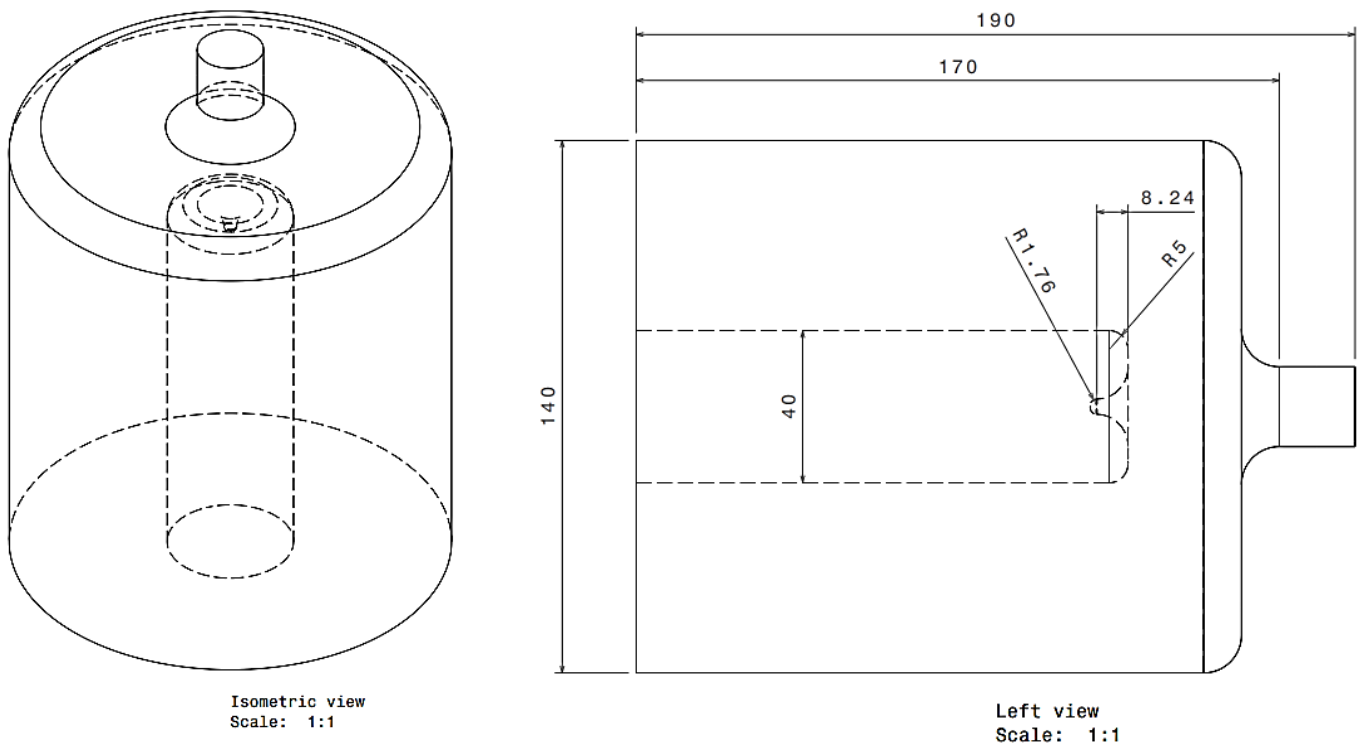


Figure 32. Initial design of copper water-cooling jacket and ground electrode created by Dominic Palubiski. All dimensions are given in mm.

Table 9. Pulse frequency and corresponding maximum reverse time values used for growth.

Pulse frequency (kHz)	Reverse time (μ s)
75	5
100	4.4
125	3.6
150	2.9

Table 10. Growth conditions used for each run of the Taguchi optimisation. The growth rates calculated for runs 5, 9 and 14 were discounted from analysis and not included in the table, due to huge rates which were based upon images from what was evidently old growth. As the growth duration did not last long enough for the voltage and current to reach a stable value, the values were not recorded for runs 5 and 13.

Run No.	Pressure (Torr)	Power (kW)	Pulse Frequency (kHz)	Ar Flow Rate (sccm)	Ar conc. (%)	CH ₄ Flow Rate (sccm)	CH ₄ conc. (%)	Voltage (V)	Current (A)	Duration (min)	Growth rate ($\mu\text{m h}^{-1}$)	
											Rate	Error (Std. Dev.)
1	130	3.70	75	0	0.0	5	1.0	450	8.2	60	4.6	0.8
2	130	3.85	100	5	1.0	10	1.9	420	9.2	60	4.0	2.9
3	130	4.00	125	10	1.9	15	2.9	430	9.3	60	5.7	1.6
4	130	4.15	150	20	3.7	20	3.7	420	9.9	60	8.0	2.4
5	175	3.70	100	10	1.9	20	3.8	/	/	8	/	/
6	175	3.85	75	20	3.7	15	2.8	470	8.2	30	3.1	0.8
7	175	4.00	150	0	0.0	10	2.0	400	10.0	20	0.0	0.0
8	175	4.15	125	5	1.0	5	1.0	415	10.0	60	2.9	2.1
9	200	3.70	125	20	3.8	10	1.9	423	8.7	30	/	/
10	200	3.85	150	10	1.9	5	1.0	430	9.0	30	3.4	1.0
11	200	4.00	75	5	1.0	20	3.8	480	8.3	25	0.0	0.0
12	200	4.15	100	0	0.0	15	2.9	475	8.7	30	0.0	0.0
13	225	3.70	150	5	1.0	15	2.9	/	/	2	0.0	0.0
14	225	3.85	125	0	0.0	20	3.8	460	8.4	5.5	/	/
15	225	4.00	100	20	3.8	5	1.0	410	9.8	9	0.0	0.0
16	225	4.15	75	10	1.9	10	1.9	460	9.0	30	1.1	0.7

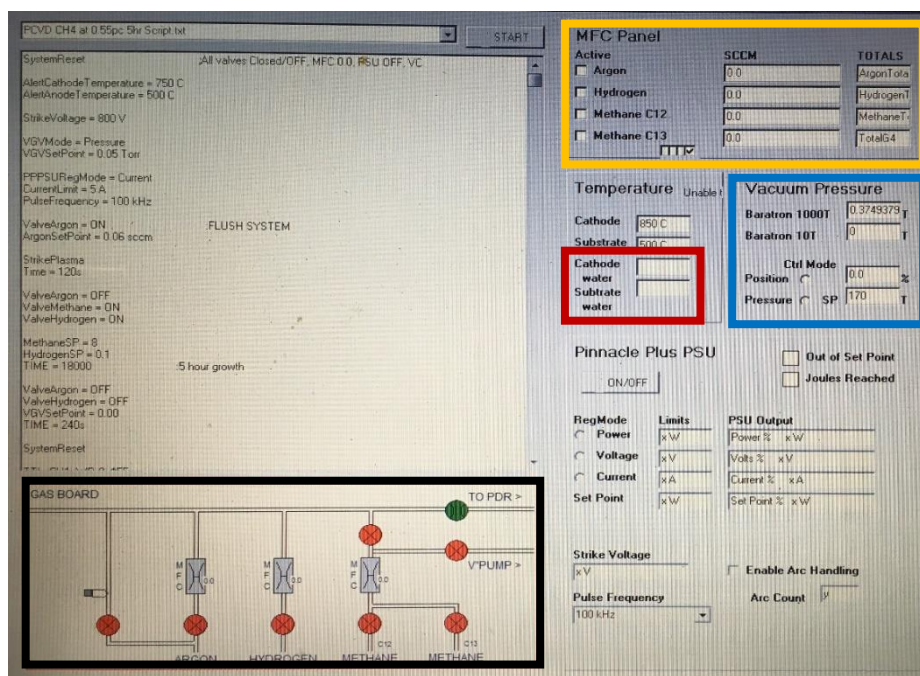


Figure 33. Image of the program used to control the reactor. The black box highlights the open (green) or closed (red) positions of the valves for gas entry to the reactor (shown open in green here). The yellow box highlights the entry boxes for the gas flow rates. The red box highlights the temperature of the water coming from the substrate and cathode. The blue box highlights the pressure of the system and the entry box for the pressure set point. The rest of the details on displayed on the program are not useful and can be ignored.

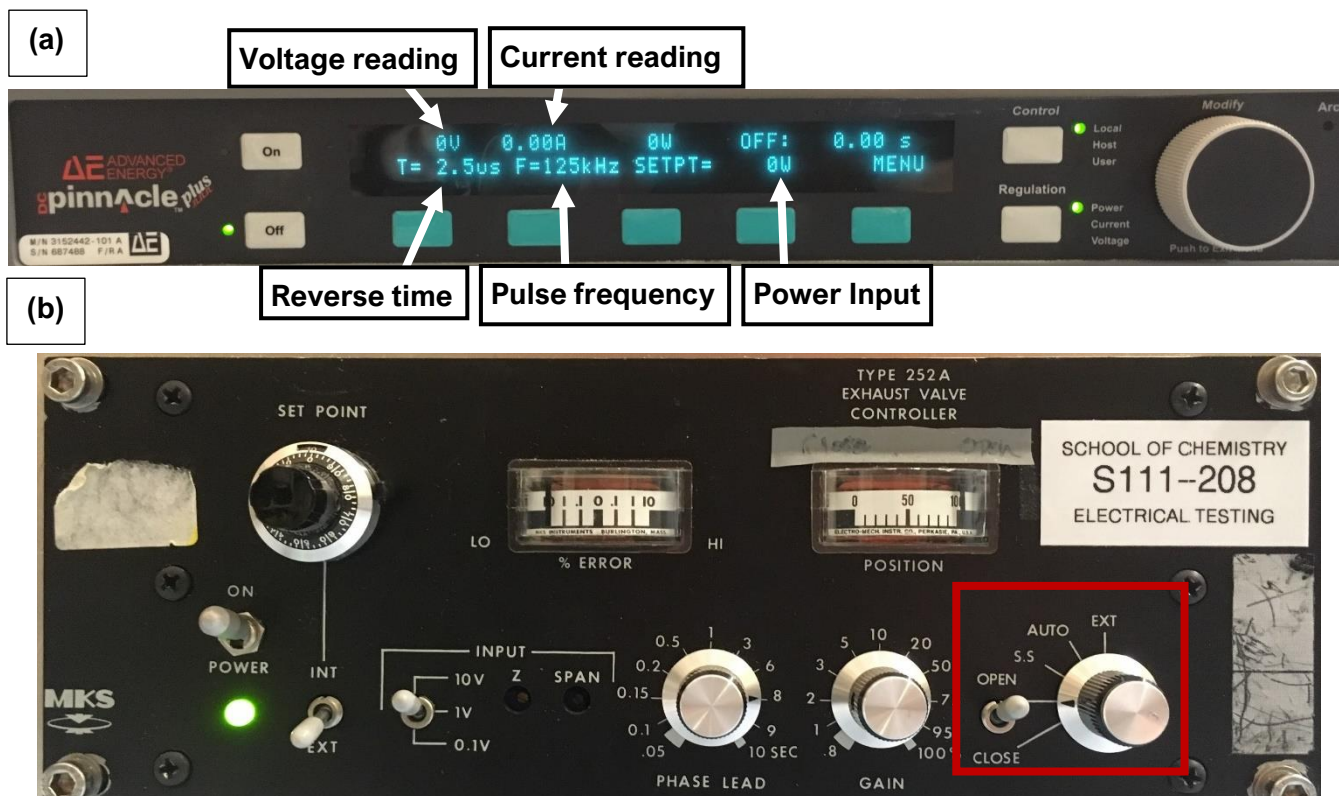


Figure 34. Images show the power (a) and butterfly vacuum control valve (b) control panels. The top image shows control over the reverse time, pulse frequency and power input and displays reading values for the voltage and current. The bottom image highlights the dial to open ('OPEN') and close ('CLOSE') the butterfly valve, and to shift the system to computer control the position of the butterfly valve ('EXT') to reach the set point pressure.

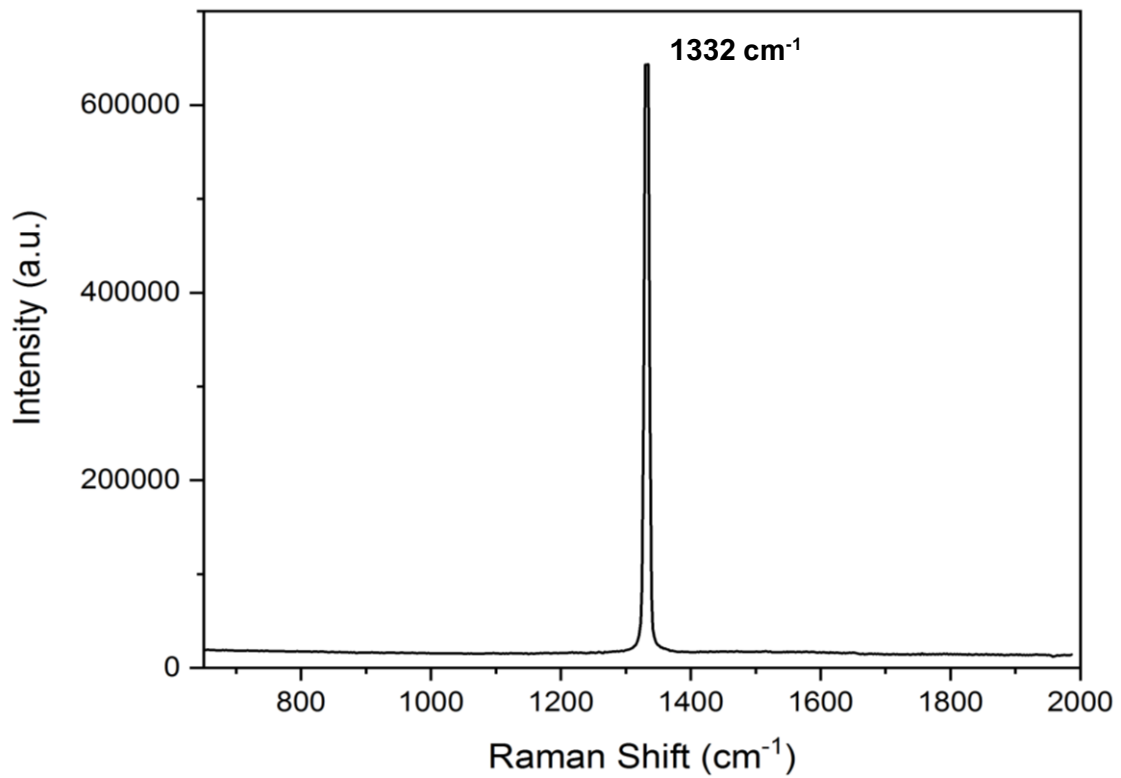


Figure 35. Raman spectrum of diamond taken for calibration of the Raman instrument.

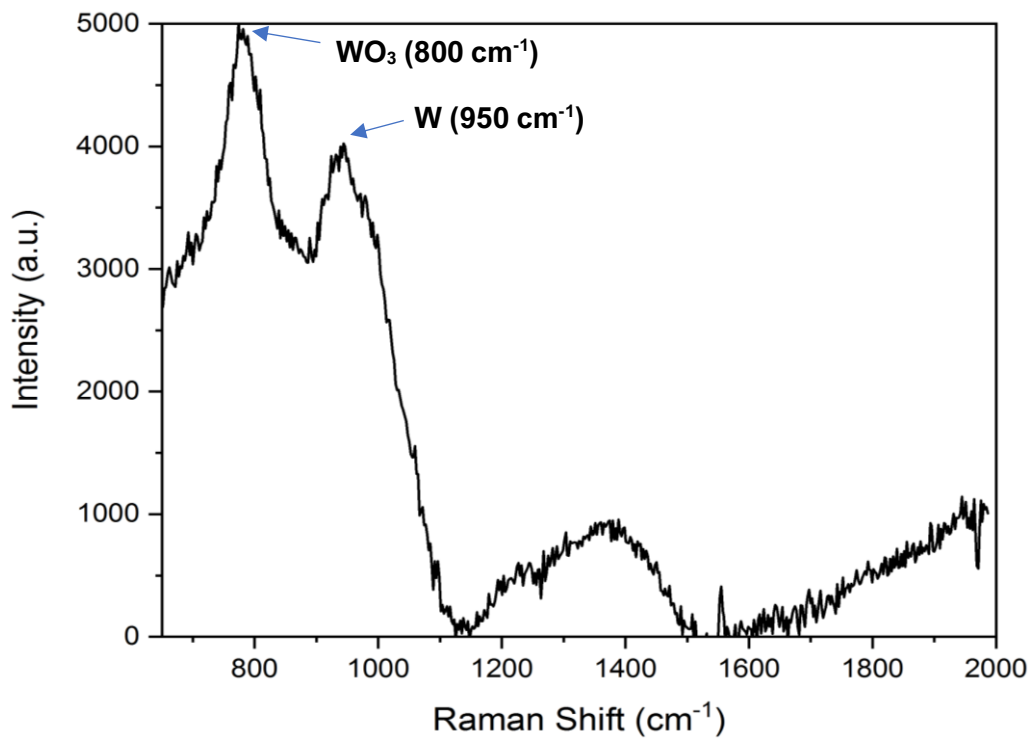


Figure 36. Raman spectrum of clean tungsten substrate. The features at 800 cm⁻¹ and 950 cm⁻¹ arise from tungsten oxide and tungsten, respectively.^[131,132]

References

- 1 K. Belay, Z. Etzel, D. G. Onn and T. R. Anthony, *J. Appl. Phys.*, 1996, **79**, 8336–8340.
- 2 S. E. Haggerty, *Nature*, 1986, **320**, 34–38.
- 3 J. J. Gracio, Q. H. Fan and J. C. Madaleno, *J. Phys. D. Appl. Phys.*, 2010, **43**, 374017.
- 4 H. Holloway, K. C. Hass, M. A. Tamor, T. R. Anthony and W. F. Banholzer, *Phys. Rev. B*, 1991, **44**, 7123–7126.
- 5 T. R. Anthony, W. F. Banholzer, J. F. Fleischer, L. Wei, P. K. Kuo, R. L. Thomas and R. W. Pryor, *Phys. Rev. B*, 1990, **42**, 1104–1111.
- 6 P. T. Moseley, D. A. J. Rand and K. Peters, *J. Power Sources*, 2015, **295**, 268–274.
- 7 C. D. Clark, P. J. Dean and P. V. Harris, *Proc. R. Soc. London. Ser. A. Math. Phys. Sci.*, 1964, **277**, 312 LP-329.
- 8 M. H. Grimsditch and A. K. Ramdas, *Phys. Rev. B*, 1975, **11**, 3139–3148.
- 9 A. T. Collins, S. C. Lawson, G. Davies and H. Kanda, *Phys. Rev. Lett.*, 1990, **65**, 891–894.
- 10 Poco Graphite, Properties and Characterisitcs of Graphite, <http://poco.com/Portals/0/Literature/Semiconductor/IND-109441-0115.pdf>, (accessed 16 December 2018).
- 11 J. R. Cost, K. R. Janowski and R. C. Rossi, *Philos. Mag. A J. Theor. Exp. Appl. Phys.*, 1968, **17**, 851–854.
- 12 T. R. Anthony and W. F. Banholzer, *Diam. Relat. Mater.*, 1992, **1**, 717–726.
- 13 J. W. Bray and T. R. Anthony, *Zeitschrift für Phys. B Condens. Matter*, 1991, **84**, 51–57.
- 14 A. M. Abyzov, S. V. Kidalov and F. M. Shakhov, *Appl. Therm. Eng.*, 2012, **48**, 72–80.
- 15 T. Schubert, Ł. Ciupiński, W. Zieliński, A. Michalski, T. Weißgärber and B. Kieback, *Scr. Mater.*, 2008, **58**, 263–266.
- 16 B. J. Baliga, *IEEE Electron Device Lett.*, 1989, **10**, 455–457.
- 17 M. N. Yoder, *IEEE Trans. Electron Devices*, 1996, **43**, 1633–1636.
- 18 T. Ruf, M. Cardona, H. Sternschulte, S. Wahl, K. Thonke, R. Sauer, P. Pavone and T. R. Anthony, *Solid State Commun.*, 1998, **105**, 311–316.
- 19 J. E. Bloor and S. Gartside, *Nature*, 1959, **184**, 1313.
- 20 X. Chen, F. Tian, C. Persson, W. Duan and N. Chen, *Sci. Rep.*, 2013, **3**, 3046.
- 21 Nuclear Decommissioning Authority, *Radioactive Wastes in the UK: A Summary of the 2016 Inventory*, 2017.
- 22 Cabot Institute for the Environment, ‘Diamond-age’ of power generation as nuclear batteries developed, <http://www.bristol.ac.uk/cabot/what-we-do/more-case-studies/2016/diamond-battery.html>, (accessed 8 April 2019).
- 23 M. A. Prelas, C. L. Weaver, M. L. Watermann, E. D. Lukosi, R. J. Schott and D. A. Wisniewski, *Prog. Nucl. Energy*, 2014, **75**, 117–148.

- 24 H. Guo and A. Lal, in *TRANSDUCERS '03. 12th International Conference on Solid-State Sensors, Actuators and Microsystems. Digest of Technical Papers (Cat. No.03TH8664)*, 2003, vol. 1, pp. 36–39 vol.1.
- 25 V. Bormashov, S. Troschiev, A. Volkov, S. Tarelkin, E. Korostylev, A. Golovanov, M. Kuznetsov, D. Teteruk, N. Kornilov, S. Terentiev, S. Buga and V. Blank, *Phys. status solidi*, 2015, **212**, 2539–2547.
- 26 C. Delfaure, M. Pomorski, J. de Sanoit, P. Bergonzo and S. Saada, *Appl. Phys. Lett.*, 2016, **108**, 252105.
- 27 A. Jayaraman, *Rev. Mod. Phys.*, 1983, **55**, 65–108.
- 28 F. Datchi, A. Dewaele, P. Loubeyre, R. Letoullec, Y. Le Godec and B. Canny, *High Press. Res.*, 2007, **27**, 447–463.
- 29 D. Schiferl, M. Nicol, J. M. Zaug, S. K. Sharma, T. F. Cooney, S.-Y. Wang, T. R. Anthony and J. F. Fleischer, *J. Appl. Phys.*, 1997, **82**, 3256–3265.
- 30 N. Chertkova, S. Yamashita, E. Ito and A. Shimojuku, *Mineral. Mag.*, 2014, **78**, 1677–1685.
- 31 E. Tyukalova, B. Kulnitskiy, I. Perezhogin, A. Kirichenko and V. Blank, *Eur. Microsc. Congr. 2016 Proc.*, 2016.
- 32 P. May and J. Thompson, *Philos. Trans. R. Soc. London. Ser. A Math. Phys. Eng. Sci.*, 2000, **358**, 473–495.
- 33 W. Banholzer, *Surf. Coatings Technol.*, 1992, **53**, 1–12.
- 34 C. J. Chu, M. P. D'Evelyn, R. H. Hauge and J. L. Margrave, *J. Mater. Res.*, 1990, **5**, 2405–2413.
- 35 T. I. Hukka, T. A. Pakkanen and M. P. D'Evelyn, *J. Phys. Chem.*, 1994, **98**, 12420–12430.
- 36 P. Carey, Master's Thesis, Dublin City University, 1989.
- 37 P. W. May, J. A. Smith and Y. A. Mankelevich, *Diam. Relat. Mater.*, 2006, **15**, 345–352.
- 38 S. Sciortino, S. Lagomarsino, F. Pieralli, E. Borchini and E. Galvanetto, *Diam. Relat. Mater.*, 2002, **11**, 573–578.
- 39 K. Benzhour, J. Szatkowski, F. Rozploch and K. Stec, *Acta Phys. Pol. A*, 2010, **118**, 447–449.
- 40 A. Tallaire, C. Rond, F. Bénédict, O. Brinza, J. Achard, F. Silva and A. Gicquel, *Phys. status solidi*, 2011, **208**, 2028–2032.
- 41 Y.-S. Han, Y.-K. Kim and J.-Y. Lee, *Thin Solid Films*, 1997, **310**, 39–46.
- 42 H. Yamada, A. Chayahara and Y. Mokuno, *Diam. Relat. Mater.*, 2018, **87**, 143–148.
- 43 C. O'Neal and R. S. Brokaw, *Phys. Fluids*, 1962, **5**, 567–574.
- 44 W. Zhu, A. Inspektor, A. R. Badzian, T. McKenna and R. Messier, *J. Appl. Phys.*, 1990, **68**, 1489–1496.
- 45 A. B. Murphy, *Plasma Chem. Plasma Process.*, 2000, **20**, 279–297.
- 46 J. C. Angus, H. A. Will and W. S. Stanko, *J. Appl. Phys.*, 1968, **39**, 2915–2922.
- 47 F. P. Bundy, *J. Geophys. Res. Solid Earth*, 1980, **85**, 6930–6936.
- 48 J. Rantala, Diamonds are a Thermal Designer's Best Friends, <https://www.electronics->

cooling.com/2002/02/diamonds-are-a-thermal-designers-best-friends/, (accessed 14 January 2019).

- 49 A. P. Bolshakov, V. G. Ralchenko, V. Y. Yurov, A. F. Popovich, I. A. Antonova, A. A. Khomich, E. E. Ashkinazi, S. G. Ryzhkov, A. V Vlasov and A. V Khomich, *Diam. Relat. Mater.*, 2016, **62**, 49–57.
- 50 Y. A. Mankelevich and P. W. May, *Diam. Relat. Mater.*, 2008, **17**, 1021–1028.
- 51 A. F. Popovich, V. G. Ralchenko, V. K. Balla, A. K. Mallik, A. A. Khomich, A. P. Bolshakov, D. N. Sovyk, E. E. Ashkinazi and V. Y. Yurov, *Plasma Sci. Technol.*, 2017, **19**, 35503.
- 52 K. J. Sankaran, P. T. Joseph, H. C. Chen, N. H. Tai and I. N. Lin, *Diam. Relat. Mater.*, 2011, **20**, 232–237.
- 53 M. Hiramatsu, K. Murata, M. Naito, S. Takashima, H. Kondo and M. Hori, *Radical density measurements in microwave plasma with carbon-containing gases used for carbon nanotube and nanocrystalline diamond film growth*, 2019.
- 54 R. M. Nor, S. A. Bakar, T. M. Thandavan and M. Rusop, *Adv. Struct. Mater.*, 2011, **5**, 195–217.
- 55 P. Hartmann, R. Haubner and B. Lux, *Diam. Relat. Mater.*, 1996, **5**, 850–856.
- 56 V. I. Konov, A. A. Smolin, V. G. Ralchenko, S. M. Pimenov, E. D. Obraztsova, E. N. Loubnin, S. M. Metev and G. Sepold, *Diam. Relat. Mater.*, 1995, **4**, 1073–1078.
- 57 M. Noda and M. Umeno, *Diam. Relat. Mater.*, 2005, **14**, 1791–1794.
- 58 C. Corbella, M. Vives, G. Oncins, C. Canal, J. L. Andújar and E. Bertran, *Diam. Relat. Mater.*, 2004, **13**, 1494–1499.
- 59 A. Bendavid, P. J. Martin, C. Comte, E. W. Preston, A. J. Haq, F. S. Magdon Ismail and R. K. Singh, *Diam. Relat. Mater.*, 2007, **16**, 1616–1622.
- 60 V. V. S. S. Srikanth, *Proc. Inst. Mech. Eng. Part C J. Mech. Eng. Sci.*, 2011, **226**, 303–318.
- 61 V. Taillandier, PhD Thesis, University of Leicester, 2013.
- 62 G. Richard Werner, PhD Thesis, Cornell University, 2004.
- 63 F. Massines, N. Gherardi, N. Naudé and P. Ségur, *Plasma Phys. Control. Fusion*, 2005, **47**, B577–B588.
- 64 D. Xiao, ed. D. Xiao, Springer Berlin Heidelberg, Berlin, Heidelberg, 2016, pp. 47–88.
- 65 C. L. Wadhwa, *High Voltage Engineering*, New Age International, New Delhi, 2nd edn., 2007.
- 66 M. Lieberman and A. Lichtenberg, in *Principles of Plasma Discharges and Materials Processing*, 2nd edn., 2005, pp. 535–569.
- 67 M. Noda, H. Kusakabe, K. Taniguchi and S. Maruno, *Jpn. J. Appl. Phys.*, 1994, **33**, 4400–4403.
- 68 A. Hatta, K. Kadota, Y. Mori, T. Ito, T. Sasaki, A. Hiraki and S. Okada, *Appl. Phys. Lett.*, 1995, **66**, 1602–1604.
- 69 M. Lieberman and A. Lichtenberg, in *Principles of Plasma Discharges and Materials Processing*, 2nd edn., 2005, pp. 327–386.
- 70 Advanced Energy, Pinnacle Plus+ 10 kW Power Supply 325 VDC-800 VDC User Manual, <http://www.ptb-sales.com/xtra/aetype/3152436-348.pdf>, (accessed 11 April 2019).

- 71 V. Czitrom, *Am. Stat.*, 1999, **53**, 126–131.
- 72 G. Taguchi, *Introduction to Quality Engineering: Designing Quality into Products and Processes*, Asian Productivity Organisation, Tokyo, 1986.
- 73 R. Unal and E. B. Dean, in *Proceedings of the International Society of Parametric Analyst 13th Annual*, 1991.
- 74 R. A. Fisher, *J. Minist. Agric. Gt. Britain*, 1926, 503–513.
- 75 R. A. Fisher, *The Design of Experiments*, Oliver & Boyd, Oxford, England, 1935.
- 76 C. Zang, M. I. Friswell and J. E. Mottershead, *Comput. Struct.*, 2005, **83**, 315–326.
- 77 W. Y. Fowlkes, C. M. Creveling and J. Derimiggio, *Engineering methods for robust product design : using Taguchi methods in technology and product development*, Addison-Wesley Pub. Co., 1995.
- 78 A. O. Osayi, E. A. P. Egbe and S. A. Lawal, *Am. J. Mech. Eng.*, 2015, **3**, 93–97.
- 79 R. K. Ghadai, K. Kalita, S. C. Mondal and B. P. Swain, *Mater. Manuf. Process.*, 2018, **33**, 1905–1913.
- 80 T. P. Singh and V. S. Jatti, *Part. Sci. Technol.*, 2015, **33**, 119–123.
- 81 E. Salgueiredo, M. Amaral, M. A. Neto, A. J. S. Fernandes, F. J. Oliveira and R. F. Silva, *Vacuum*, 2011, **85**, 701–704.
- 82 N. Ali, V. F. Neto, S. Mei, G. Cabral, Y. Kousar, E. Titus, A. A. Ogwu, D. S. Misra and J. Gracio, *Thin Solid Films*, 2004, **469–470**, 154–160.
- 83 D. R. Palubiski, Master's Thesis, University of Bristol, 2016.
- 84 E. Smith, Master's Thesis, University of Bristol, 2017.
- 85 H. Harris, Master's Thesis, University of Bristol, 2018.
- 86 J. Sulé-Suso, N. R. Forsyth, V. Untereiner and G. D. Sockalingum, *Trends Biotechnol.*, 2014, **32**, 254–262.
- 87 T. Ando, M. Ishii, M. Kamo and Y. Sato, *J. Chem. Soc. Faraday Trans.*, 1993, **89**, 1783–1789.
- 88 R. Vogelgesang, A. D. Alvarenga, H. Kim, A. K. Ramdas, S. Rodriguez, M. Grimsditch and T. R. Anthony, *Phys. Rev. B*, 1998, **58**, 5408–5416.
- 89 K. Havancsák, High-Resolution Scanning Electron Microscopy, <http://www.technoorg.hu/news-and-events/articles/high-resolution-scanning-electron-microscopy-1/>, (accessed 14 March 2019).
- 90 P. W. Hawkes and L. Reimer, *Scanning Electron Microscopy: Physics of Image Formation and Microanalysis*, Springer Berlin Heidelberg, 2013.
- 91 X. Jia, N. Huang, G. Yuning, L. Liu, P. Li, Z. Zhai, B. Yang, Z. Yuan, D. Shi and X. Jiang, *Growth behavior of CVD diamond films with enhanced electron field emission properties over a wide range of experimental parameters*, 2018, vol. 34.
- 92 I.-N. Lin, H.-C. Chen, C.-S. Wang, Y.-R. Lee and C.-Y. Lee, *CrystEngComm*, 2011, **13**, 6082–6089.
- 93 W. G. Schrenk, ed. W. G. Schrenk, Springer US, Boston, MA, 1975, pp. 211–242.

- 94 J. W. Coburn and M. Chen, *J. Appl. Phys.*, 1980, **51**, 3134–3136.
- 95 D. J. Kalnicky, R. N. Kniseley and V. A. Fassel, *Spectrochim. Acta Part B At. Spectrosc.*, 1975, **30**, 511–525.
- 96 E. Restrepo and A. Devia, *J. Vac. Sci. Technol. A*, 2004, **22**, 377–382.
- 97 Y. Liao, C. H. Li, Z. Y. Ye, C. Chang, G. Z. Wang and R. C. Fang, *Diam. Relat. Mater.*, 2000, **9**, 1716–1721.
- 98 J. Ma, M. N. R. Ashfold and Y. A. Mankelevich, *J. Appl. Phys.*, 2009, **105**, 43302.
- 99 A. Rousseau, A. Granier, G. Gousset and P. Leprince, *J. Phys. D. Appl. Phys.*, 1994, **27**, 1412–1422.
- 100 R. A. Gottscho and V. M. Donnelly, *J. Appl. Phys.*, 1984, **56**, 245–250.
- 101 M. Abdel-Rahman, V. S. der Gathen, T. Gans, K. Niemi and H. F. Döbele, *Plasma Sources Sci. Technol.*, 2006, **15**, 620–626.
- 102 A. Gicquel, M. Chenevier, K. Hassouni, A. Tserepi and M. Dubus, *J. Appl. Phys.*, 1998, **83**, 7504–7521.
- 103 T. Bauer, M. Schreck, F. Hörmann, A. Bergmaier, G. Dollinger and B. Stritzker, *Diam. Relat. Mater.*, 2002, **11**, 493–498.
- 104 School of Physics at the University of Bristol, The Bristol NanoESCA Laboratory, <http://www.bristol.ac.uk/physics/facilities/nanoesca/>, (accessed 19 March 2019).
- 105 P. W. May, H. Dominguez Andrade, M. Z. Othman, K. M. O'Donnell, J. H. Lay, N. A. Fox, J. Morin and O. Renault, *Int. J. Nanotechnol.*, 2014, **11**, 796–807.
- 106 G. Wan, M. Cattelan and N. A. Fox, *J. Phys. Chem. C*, 2019, **123**, 4168–4177.
- 107 W. Swiech, G. H. Fecher, C. Ziethen, O. Schmidt, G. Schönhense, K. Grzelakowski, C. M. Schneider, R. Frömter, H. P. Oepen and J. Kirschner, *J. Electron Spectros. Relat. Phenomena*, 1997, **84**, 171–188.
- 108 S.-K. Mo, *Angle-resolved photoemission spectroscopy for the study of two-dimensional materials*, 2017, vol. 4.
- 109 M. H. Hoegen, A. Al-Falou, H. Pietsch, B. H. Müller and M. Henzler, *Surf. Sci.*, 1993, **298**, 29–42.
- 110 H. Konno, eds. M. Inagaki and F. B. T.-M. S. and E. of C. Kang, Butterworth-Heinemann, 2016, pp. 153–171.
- 111 D. N. Belton, S. J. Harris, S. J. Schmieg, A. M. Weiner and T. A. Perry, *Appl. Phys. Lett.*, 1989, **54**, 416–417.
- 112 K. Ohashi, T. Roskopf, H. Watanabe, M. Loretz, Y. Tao, R. Hauert, S. Tomizawa, T. Ishikawa, J. Ishi-Hayase, S. Shikata, C. L. Degen and K. M. Itoh, *Nano Lett.*, 2013, **13**, 4733–4738.
- 113 S. Porro, G. De Temmerman, S. Lisgo, P. John, I. Villalpando, J. W. Zimmer, B. Johnson and J. I. B. Wilson, *Diam. Relat. Mater.*, 2009, **18**, 740–744.
- 114 W.-S. Lee, K.-W. Chae, K. Y. Eun and Y.-J. Baik, *Diam. Relat. Mater.*, 2001, **10**, 2220–2224.
- 115 K.-W. Chae, Y.-J. Baik, J.-K. Park and W.-S. Lee, *Diam. Relat. Mater.*, 2010, **19**, 1168–1171.
- 116 A. Sawabe, H. Yasuda, T. Inuzuka and K. Suzuki, *Appl. Surf. Sci.*, 1988, **33–34**, 539–545.

- 117 H. D. Young, *University Physics*, Addison Wesley, 7th edn., 1992.
- 118 R. Haubner and B. Lux, *Int. J. Refract. Met. Hard Mater.*, 2002, **20**, 93–100.
- 119 A. Boudina, E. Fitzer and G. Wahl, *Diam. Relat. Mater.*, 1992, **1**, 248–254.
- 120 K. Suzuki, A. Sawabe, H. Yasuda and T. Inuzuka, *Appl. Phys. Lett.*, 1987, **50**, 728–729.
- 121 J. Achard, A. Tallaire, R. Sussmann, F. Silva and A. Gicquel, *J. Cryst. Growth*, 2005, **284**, 396–405.
- 122 The BOC Group, Methane MSDS, https://www.boconline.co.uk/en/images/tg_8321_methane_tcm410-61346.pdf, (accessed 26 March 2019).
- 123 H. C. Shih, C. P. Sung and W. L. Fan, *Surf. Coatings Technol.*, 1992, **54–55**, 380–386.
- 124 Sigma Aldrich, Methane 13C, <https://www.sigmaaldrich.com/catalog/substance/methane13c1704653248511?lang=en®ion=GB>, (accessed 22 March 2019).
- 125 The BOC Group, Methane N4.5 (Research Grade CH₄) Cylinder, <https://www.boconline.co.uk/shop/en/uk/bc-100lts-rg-methane-112001>, (accessed 22 March 2019).
- 126 I. E. Alekseev, V. V Darmograi and V. V Lazarev, *Radiochemistry*, 2010, **52**, 451–453.
- 127 F. C. Nix and D. MacNair, *Phys. Rev.*, 1942, **61**, 74–78.
- 128 J. Filik, *Spectrosc. Eur.*, 2005, **17**, 10–17.
- 129 Thermo Fisher Scientific, Characterizing Carbon Materials with Raman Spectroscopy, <https://assets.thermofisher.com/TFS-Assets/CAD/Application-Notes/D19504~.pdf>, (accessed 4 March 2019).
- 130 A. Dychalska, P. Popielarski, W. Franków, K. Fabisiak, K. Paprocki and M. Szybowicz, *Mater. Sci.*, 2015, **33**, 799–805.
- 131 R. S. Lillard, G. S. Kanner and D. P. Butt, *J. Electrochem. Soc.*, 1998, **145**, 2718–2725.
- 132 A. Warren, A. Nylund and I. Olefjord, *Int. J. Refract. Met. Hard Mater.*, 1996, **14**, 345–353.
- 133 M. A. Pimenta, G. Dresselhaus, M. S. Dresselhaus, L. G. Cançado, A. Jorio and R. Saito, *Phys. Chem. Chem. Phys.*, 2007, **9**, 1276–1290.
- 134 A. C. Ferrari and J. Robertson, *Phys. Rev. B*, 2000, **61**, 14095–14107.
- 135 D. D. L. Chung, *J. Mater. Sci.*, 2002, **37**, 1475–1489.
- 136 S. Han, L. S. Pan and D. R. Kania, eds. L. S. Pan and D. R. Kania, Springer US, Boston, MA, 1995, pp. 241–284.
- 137 K. Kobashi, K. Nishimura, Y. Kawate and T. Horiuchi, *Phys. Rev. B*, 1988, **38**, 4067–4084.
- 138 J. Laimer and S. Matsumoto, *Int. J. Refract. Met. Hard Mater.*, 1996, **14**, 179–184.
- 139 J. Laimer, M. Shimokawa and S. Matsumoto, *Diam. Relat. Mater.*, 1994, **3**, 231–238.
- 140 R. Haubner, *Nanodiamond*, 2014, 253–267.
- 141 S. Bühlmann, E. Blank, R. Haubner and B. Lux, *Diam. Relat. Mater.*, 1999, **8**, 194–201.

- 142 X. Li, J. Perkins, R. Collazo, R. J. Nemanich and Z. Sitar, *Diam. Relat. Mater.*, 2006, **15**, 1784–1788.
- 143 A. Mohanta, B. Lanfant, M. Asfaha and M. Leparoux, *J. Phys. Conf. Ser.*, 2017, **825**, 12010.
- 144 L. Nemes, A. M. Keszler, C. G. Parigger, J. O. Hornkohl, H. A. Michelsen and V. Stakhursky, *Appl. Opt.*, 2007, **46**, 4032–4040.
- 145 H. Zhou, J. Watanabe, M. Miyake, A. Ogino, M. Nagatsu and R. Zhan, *Diam. Relat. Mater.*, 2007, **16**, 675–678.
- 146 Y. Honda, A. Álvaro-González, A. Nezu and H. Akatsuka, *Energy Procedia*, 2017, **131**, 312–318.
- 147 I. B. Denysenko, S. Xu, J. D. Long, P. P. Rutkevych, N. A. Azarenkov and K. Ostrikov, *J. Appl. Phys.*, 2004, **95**, 2713–2724.
- 148 P. Fazekas, A. Keszler, E. Bódis, E. Drotár, S. Klébert, Z. Károly and J. Szépvölgyi, *Open Chem.*, 2015, **13**, 549–556.
- 149 W. L. Wiese, J. W. Brault, K. Danzmann, V. Helbig and M. Kock, *Phys. Rev. A*, 1989, **39**, 2461–2471.
- 150 D. L. Crintea, U. Czarnetzki, S. Iordanova, I. Koleva and D. Luggenhölscher, *J. Phys. D. Appl. Phys.*, 2009, **42**, 45208.